A&A 646, A30 (2021)
https://doi.org/10.1051/0004-6361/202038930

Astronomy & Astrophysics

The formation of ultra-massive carbon-oxygen core white dwarfs and their evolutionary and pulsational properties⋆

Leandro G. Althaus[1,2], Pilar Gil Pons[3], Alejandro H. Córsico[1,2], Marcelo Miller Bertolami[1,2], Francisco De Gerónimo[1,2], María E. Camisassa[1,2,3], Santiago Torres[3,4], Jordi Gutierrez[3], and Alberto Rebassa-Mansergas[3,4]

[1] Grupo de Evolución Estelar y Pulsaciones, Facultad de Ciencias Astronómicas y Geofísicas, Universidad Nacional de La Plata, Paseo del Bosque s/n, 1900 La Plata, Argentina
e-mail: althaus@fcaglp.unlp.edu.ar
[2] CCT – CONICET, Paseo del Bosque s/n,1900 La Plata, Argentina
[3] Departament de Física, Universitat Politècnica de Catalunya, c/Esteve Terrades 5, 08860 Castelldefels, Spain
[4] Institute for Space Studies of Catalonia, c/Gran Capita 2–4, Edif. Nexus 104, 08034 Barcelona, Spain

Received 14 July 2020 / Accepted 18 November 2020

ABSTRACT

Context. The existence of ultra-massive white dwarf stars, $M_{\rm WD} \gtrsim 1.05\,M_{\odot}$, has been reported in several studies. These white dwarfs are relevant for the role they play in type Ia supernova explosions, the occurrence of physical processes in the asymptotic giant-branch phase, the existence of high-field magnetic white dwarfs, and the occurrence of double-white-dwarf mergers.
Aims. We aim to explore the formation of ultra-massive, carbon-oxygen core white dwarfs resulting from single stellar evolution. We also intend to study their evolutionary and pulsational properties and compare them with those of the ultra-massive white dwarfs with oxygen-neon cores resulting from carbon burning in single progenitor stars, and with binary merger predictions. The aim is to provide a theoretical basis that can eventually help to discern the core composition of ultra-massive white dwarfs and the circumstances of their formation.
Methods. We considered two single-star evolution scenarios for the formation of ultra-massive carbon-oxygen core white dwarfs, which involve the rotation of the degenerate core after core helium burning and reduced mass-loss rates in massive asymptotic giant-branch stars. We find that reducing standard mass-loss rates by a factor larger than 5−20 yields the formation of carbon-oxygen cores more massive than $1.05\,M_{\odot}$ as a result of the slow growth of carbon-oxygen core mass during the thermal pulses. We also performed a series of evolutionary tests of solar-metallicity models with initial masses between 4 and $9.5\,M_{\odot}$ and with different core rotation rates. We find that ultra-massive carbon-oxygen core white dwarfs are formed even for the lowest rotation rates we analyzed, and that the range of initial masses leading to these white dwarfs widens as the rotation rate of the core increases, whereas the initial mass range for the formation of oxygen-neon core white dwarfs decreases significantly. Finally, we compared our findings with the predictions from ultra-massive white dwarfs resulting from the merger of two equal-mass carbon-oxygen core white dwarfs, by assuming complete mixing between them and a carbon-oxygen core for the merged remnant.
Results. These two single-evolution scenarios produce ultra-massive white dwarfs with different carbon-oxygen profiles and different helium contents, thus leading to distinctive signatures in the period spectrum and mode-trapping properties of pulsating hydrogen-rich white dwarfs. The resulting ultra-massive carbon-oxygen core white dwarfs evolve markedly slower than their oxygen-neon counterparts.
Conclusions. Our study strongly suggests the formation of ultra-massive white dwarfs with carbon-oxygen cores from a single stellar evolution. We find that both the evolutionary and pulsation properties of these white dwarfs are markedly different from those of their oxygen-neon core counterparts and from those white dwarfs with carbon-oxygen cores that might result from double-degenerate mergers. This can eventually be used to discern the core composition of ultra-massive white dwarfs and their formation scenario.

Key words. stars: evolution – stars: interiors – white dwarfs – stars: oscillations

1. Introduction

The white dwarf (WD) state constitutes the final fate for all of the single low- and intermediate-mass stars. WD stars, which are Earth-sized electron-degenerate stellar configurations, play a major role in our understanding of the formation and evolution of stars, the history of our Galaxy and stellar populations, and the evolution of planetary systems (see Fontaine & Brassard 2008; Winget & Kepler 2008; Althaus et al. 2010a; Córsico et al. 2019a for reviews). Of particular interest is the mass distribution of WDs. Although there exists an intense debate about its exact distribution, it is generally agreed that it shows a main peak at $M_{\rm WD} \sim 0.6\,M_{\odot}$, and a smaller peak at the tail of the distribution around $M_{\rm WD} \sim 0.82\,M_{\odot}$ (e.g., Kleinman et al. 2013; Jiménez-Esteban et al. 2018). In addition, the existence of ultra-massive WDs ($M_{\rm WD} \gtrsim 1.05\,M_{\odot}$) has been reported in several studies (Castanheira et al. 2010, 2013; Hermes et al. 2013; Kepler et al. 2016; Curd et al. 2017; Hollands et al. 2020). Additionally, Rebassa-Mansergas et al. (2015) reported the existence of a clear excess in the number of hydrogen (H)-rich WDs with masses near $1\,M_{\odot}$. The interest in ultra-massive WDs is motivated by the role they play in type Ia supernovae, the occurrence of physical processes in the asymptotic giant branch (AGB) phase,

⋆ The evolutionary sequences are only available at the CDS via anonymous ftp to cdsarc.u-strasbg.fr (130.79.128.5) or via http://cdsarc.u-strasbg.fr/viz-bin/cat/J/A+A/646/A30

and the existence of high-field magnetic WDs and double-WD mergers (Dunlap & Clemens 2015; Reindl et al. 2020). Moreover, because of their very high central densities, ultra-massive WDs offer a test bed to infer and explore the theory of crystallisation thanks to the capability of asteroseismology to potentially probe the very deep interior of these stars, see Córsico et al. (2019a) for a recent review.

Ultra-massive WDs are thought to be the outcome of single stellar evolution of progenitor stars with masses higher than 6−9 $M_{\odot}$ that lose their envelope through winds before the core reaches the Chandrasekhar mass (if this happens, the result is an electron-capture supernovae; ECSN). This initial mass threshold depends on metallicity and input physics such as the treatment of convective boundaries (see Doherty et al. 2017 for a review). After helium (He) exhaustion, these stars evolve to the super asymptotic giant branch (SAGB), where core temperatures become high enough to start off-centre carbon ignition under partially degenerate conditions, leading to a carbon-burning flash with associated luminosity up to $10^9\,L_{\odot}$. This takes place when the carbon-oxygen (CO) core mass has grown to about 1.05 $M_{\odot}$ and before the thermally pulsing AGB (TP-AGB) phase is reached (see e.g., García-Berro & Iben 1994; Siess 2007; Doherty et al. 2017). The violent carbon-ignition phase is followed by the development of an inward-propagating convective flame that transforms the CO core into a degenerate oxygen-neon (ONe) core (García-Berro et al. 1997; Gil-Pons et al. 2005; Siess 2006; Doherty et al. 2010; Ventura & D'Antona 2011)[1]. In this scenario, ultra-massive WDs with stellar masses larger than $M_{\rm WD} \gtrsim 1.05\,M_{\odot}$ composed of ^{16}O and ^{20}Ne and traces of ^{23}Na and ^{24}Mg are expected to emerge (Siess 2007).

An alternative scenario for the formation of ultra-massive WDs has gained relevance in recent years. Indeed, evidence has been mounting that a fraction of single ultra-massive WDs could be the result of binary evolution channels. Recent studies point towards a substantial contribution of binary mergers to the single WD population (Toonen et al. 2017; Maoz et al. 2018). In particular, Temmink et al. (2020) conclude that, on the basis of binary population synthesis results, about 30−45% of all observable single WD more massive than 0.9 $M_{\odot}$ within 100 pc are formed through binary mergers, mostly via the merger of two WDs. In addition, based on the velocity distribution of high-mass WDs in the range 0.8−1.3 $M_{\odot}$, Cheng et al. (2020) estimate that the fraction of double-WD mergers in their sample amounts to about 20%. The result of such WD mergers remains a matter of debate. According to Yoon et al. (2007) and Lorén-Aguilar et al. (2009), the possibility that the merger remnants avoid off-centre carbon burning and become single ultra-massive WDs characterised by a CO core (hereinafter referred to as UMCO WDs) cannot be discarded. However, recent studies based on one-dimensional post merger evolutionary models (Schwab 2021) predict ultra-massive WDs with ONe cores as a result of off-centre carbon burning in the merged remnant (see also Shen et al. 2012).

Fortunately, several ultra-massive H-rich WDs (DA WDs) exhibit g(gravity)-mode pulsational instabilities (Kanaan et al. 2005; Castanheira et al. 2010, 2013; Hermes et al. 2013; Curd et al. 2017; Rowan et al. 2019), so their internal structure could be probed through asteroseismology. The study of the predicted pulsational patterns of UMCO and ONe-core WDs could eventually help to distinguish between both types of stars and place constraints on the different channels in the formation of these stars. In this sense, based on new evolutionary models computed by Camisassa et al. (2019) for the evolution of ONe-core WDs that consider new phase diagrams for ONe phase separation core upon crystallization, De Gerónimo et al. (2019) showed that the features found in the period-spacing diagrams could be used as a seismological tool to discern the core composition of pulsating ultra-massive WDs. Furthermore, on the basis of these models, Córsico et al. (2019b) carried out the first asteroseismological analysis of ultra-massive ZZ Ceti stars, focusing in particular on the stars BPM 37093, GD 518, and SDSS J0840+5222.

In this paper, we explore two possible single-evolution scenarios for the formation of UMCO WDs. One scenario exploits wind rate uncertainties during the TP-AGB phase (see e.g., Decin et al. 2019) and involves the reduction of these rates below the values given by standard prescriptions. The alternative scenario involves the occurrence of rotation in degenerate CO cores expected from the contraction of the core at the onset of the AGB phase following central He exhaustion (Dominguez et al. 1996; hereinafter Dom96). We show that both the evolutionary and pulsational properties of the UMCO WDs formed through these two single-evolution scenarios are markedly different from those of their ONe-core counterparts and from those WDs with carbon-oxygen cores that might result from double-degenerate mergers. This can eventually be used to discern the core composition of ultra-massive WDs and their origin.

The paper is organised as follows. In Sect. 2, we describe the evolutionary and pulsational codes. In Sect. 3, we present details about the scenarios we explored that lead to the formation of UMCO WDs. In Sects. 4 and 5, we describe the evolutionary and pulsational properties, respectively, of the resulting WDs. Finally, in Sect. 6, we summarise the main findings of the paper.

2. Evolutionary and pulsational codes

Three different but complementary codes were applied in the analysis carried out as part of this work. In what follows, we summarise the main input physics used in them.

The structure and composition of the UMCO WD progenitors were computed with the Monash-Mount Stromlo code MONSTAR (Wood & Faulkner 1987; Frost & Lattanzio 1996; Campbell & Lattanzio 2008), and presented in Gil-Pons et al. (2013, 2018). Here, we summarise the main input physics used. The mixing length to pressure scale height quotient is $\alpha = 1.75$. Usually, convective boundaries with MONSTAR are determined using the Schwarzschild criterion and the search for neutrality approach (Castellani et al. 1971; Frost & Lattanzio 1996). As recent calculations with MONSTAR (see e.g., Doherty et al. 2017, and references therein), mass-loss rates during the RGB phase follow the prescription of Reimers (1975) with $\eta = 0.4$. Mass loss during this part of the evolution is very modest ($\lesssim$0.05 $M_{\odot}$), and thus its effects on the overall evolution are minor. For the AGB phase, we used the standard wind-rate prescription of Vassiliadis & Wood (1993). Overshooting has not been considered. Relativistic and ion gases are treated using the fitting formulae by Beaudet & Tassoul (1971). Interior stellar opacities are from Iglesias & Rogers (1996). Low-temperature opacity tables are from Lederer & Aringer (2009) and Marigo & Aringer (2009), and they take into account variable composition effects.

For this work, we implemented a simplified approach to the effects of rotation following the treatment described in Dom96, which is based on Kippenhahn et al. (1970). This treatment provides an approximation to the inherently multi-dimensional

[1] In some cases, aborted carbon ignition results and a CO core surrounded by an ONe envelope could be expected (Doherty et al. 2010; Ventura & D'Antona 2011; Denissenkov et al. 2013).

phenomenon of rotation for one-dimensional evolutionary codes. In particular, it captures the main effect of the decrease in core pressure caused by the increase in angular velocities expected from the compression of the CO core at the onset of the AGB phase. Specifically, the hydrostatic equilibrium equation is modified inside the core by introducing the rotation parameter f as follows:

$$\frac{\mathrm{d}P}{\mathrm{d}M_{\mathrm{r}}} = -\frac{GM_{\mathrm{r}}}{4\pi\, r^4}(1-f), \tag{1}$$

where f is related to the critical velocity, $\sqrt{f} = \omega/\omega_{\mathrm{crit}}$. For the sake of simplicity, and also following Dom96, f is taken to be constant.

More sophisticated implementations of rotation exist in the literature (see i.e., Maeder & Meynet 2000; Heger & Langer 2000; Farmer et al. 2015; Limongi & Chieffi 2018; Paxton et al. 2019). However, the physics of internal angular momentum transport in stars is not well understood, and sophisticated models that allow a proper assessment of the evolution of the angular momentum in evolved low-mass stars fail to predict the observed core rotation of early red giants and clump stars (see Cantiello et al. 2014). In fact, all these approaches neglect the basic dimensionality of a rotating structure, for which a two-dimensional approach seems to be the minimum accuracy requisite (Espinosa Lara & Rieutord 2013). Hence, we rely instead on the much simpler model we have described, which is sufficient for our purposes. We stress that we do not attempt here to follow the evolution of angular momentum in prior evolutionary stages, but simply to explore the expectation for the CO-core masses and to achieve initial UMCO WD configurations for our evolving models by assuming different rotation rates during the AGB phase. As shown in Dom96, this simple treatment to simulate the presence of rotation captures the expected decrease in maximun temperature in response to a pressure decrease, favouring the formation of UMCO cores. More elaborate stellar models that include the variation of the angular momentum content of the star also predict a significant increase in the CO-core mass as a result of core rotation (see Table 1 of Georgy et al. 2013 for the case of more massive stars than those studied here). Finally, it should be mentioned that when studying SAGB stars, Farmer et al. (2015) did not point to marked differences in important aspects of carbon burning, such as ignition point masses or flame quenching locations when rotation is implemented. This is probably justified by the strong influence of the magnetic torques implemented in the work by Farmer et al. (2015), which significantly inhibited the spin-up of model cores. We note that our knowledge of this phenomenon in stellar evolution is still poor, and further research has to be done to completely understand the behaviour of magnetic fields and rotation (Gagnier et al. 2019).

The initial composition of our models was taken from Grevesse et al. (1996), and MONSOON, the postprocessing code developed at Monash University (Cannon 1993; Lugaro et al. 2004; Doherty et al. 2014), was used to perform detailed nucleosynthetic calculations. The specific version we used includes 77 species, up to ^{32}S and Fe-peak elements. It also includes a 'g' particle (Lugaro et al. 2004), which is a proxy for s-process elements. The neutron-sink approach (Jorissen & Arnould 1989; Lugaro et al. 2003; Herwig et al. 2003) allows us to account for eventual neutron captures on nuclides that are not present in our network. Most nuclear reaction rates are from the JINA reaction library (Cyburt et al. 2010). Moreover, p-captures for the NeNa-cycle and MgAl chain are from Iliadis et al. (2001), p-captures on ^{22}Ne are from Hale et al. (2002), α-captures on ^{22}Ne are from Karakas et al. (2006), and p-captures on ^{23}Na are from Hale et al. (2004).

The WD evolutionary models used in this work were computed using the LPCODE stellar evolutionary code that has been widely used to study the evolution of low-mass and WD stars (see Althaus et al. 2003, 2005, 2015; Miller Bertolami 2016 for details about the code). The LPCODE has been tested and calibrated with other stellar evolutionary codes at different evolutionary stages, such as the red giant phase (Silva Aguirre et al. 2020; Christensen-Dalsgaard et al. 2020) and the WD stage (Salaris et al. 2013). Relevant for the present work, LPCODE considers a new fully implicit treatment of time-dependent element diffusion, which includes thermal and chemical diffusion and gravitational settling (Althaus et al. 2020), outer boundary conditions provided by non-grey model atmospheres (Rohrmann et al. 2012; Camisassa et al. 2017; Rohrmann 2018), and a full treatment of energy sources, in particular the energy contribution ensuing from phase separation of core chemical species upon crystallisation. The treatment of crystallisation is based on the most up-to-date phase diagrams of Horowitz et al. (2010) for dense CO mixtures, and that of Medin & Cumming (2010) for ONe mixtures. In this work, we do not consider ^{22}Ne sedimentation. Recently, LPCODE was also used to calculate a grid of ultra-massive ONe WDs with stellar masses in the 1.10−1.29 $M_{\odot}$ range (Camisassa et al. 2019) based on detailed chemical profiles as given by 9−10.5 $M_{\odot}$ single progenitors evolved through the semi-degenerate carbon burning and the TP-AGB phases (Siess 2010). These new ultra-massive ONe models include, for the first time, the release of energy and the core chemical redistribution ensuing from the phase separation of ^{16}O and ^{20}Ne upon crystallisation, thus substantially improving previous attempts to model these stars. We wish to mention that during the WD regime, rotation was not considered.

Finally, for the pulsation analysis of our WD models, we employed the adiabatic version of the LP-PUL pulsation code described in Córsico & Althaus (2006). This code was recently employed by De Gerónimo et al. (2019) to study the pulsation properties of the ONe-core ultra-massive WD models computed by Camisassa et al. (2019) and Córsico et al. (2019b) to perform the first asteroseismological analyses of ultra-massive ZZ Ceti stars. To account for the effects of crystallisation on the pulsation spectrum of g-modes, we adopted the 'hard sphere' boundary conditions, which assume that the amplitude of the eigenfunctions of g-modes is drastically reduced below the solid-liquid interface because of the non-shear modulus of the solid, as compared with the amplitude in the fluid region (see Montgomery & Winget 1999). In our code, the inner boundary condition is not the stellar centre, but instead the mesh-point corresponding to the crystallisation front moving towards the surface (see Córsico et al. 2004, 2005, 2019b; De Gerónimo et al. 2019). The Brunt–Väisälä frequency is computed as in Tassoul et al. (1990). The computation of the Ledoux term B –a crucial amount involved in the Brunt–Väisälä frequency calculation– includes the effects of having multiple chemical species that vary in abundance.

3. The formation of UMCO WDs

In this section, we explore the formation of UMCO WDs resulting from single stellar evolution by focusing on the role of rotation and mass loss in the evolution of the degenerate CO cores of evolved AGB stars. We also considered the formation of UMCO WDs via a double-WD merger.

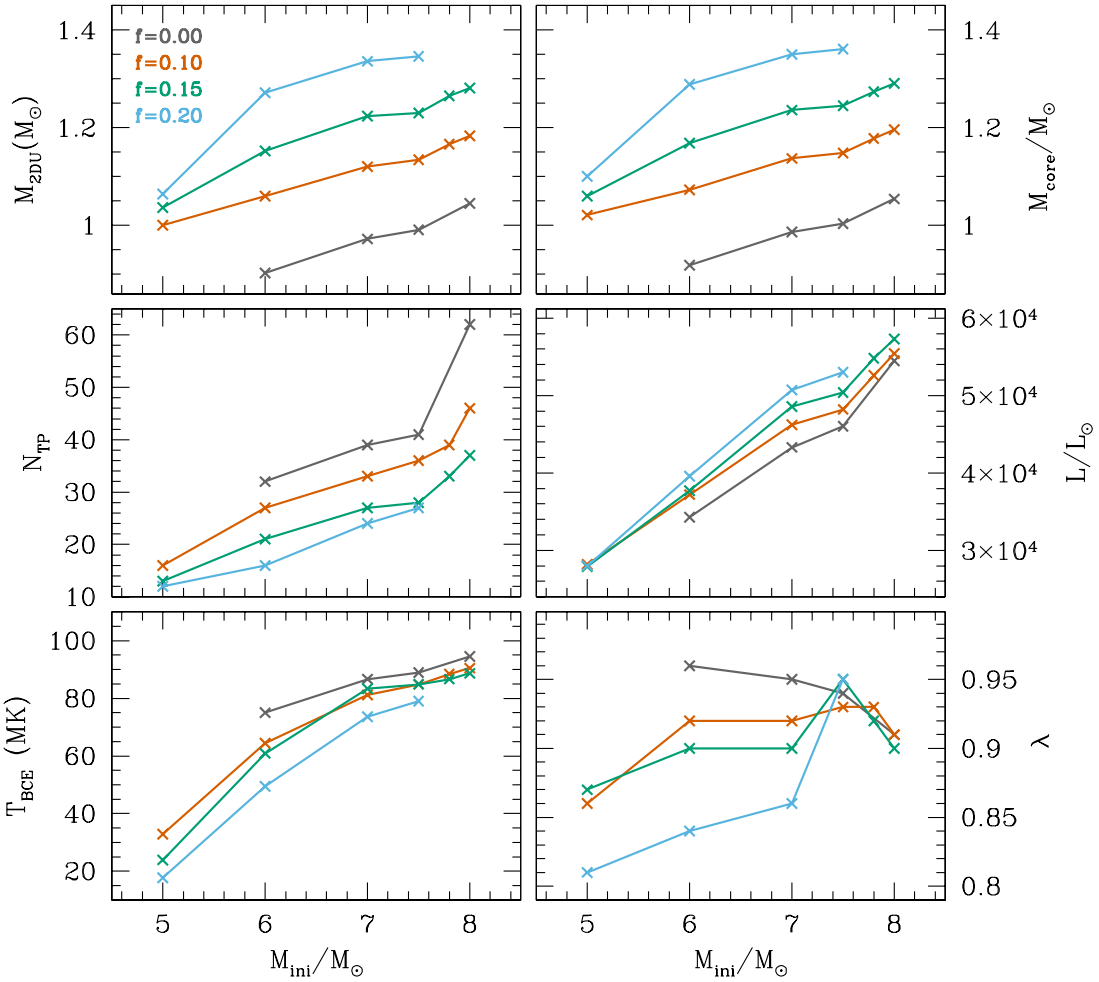

Fig. 1. *Upper panels*: H-exhausted core mass at the maximum advance of the SDU (*left*) and at the end of our calculations (*right*). *Middle panels*: number of thermal pulses of our sequences (*left*) and maximum surface luminosity values reached during the TP-AGB (*right*). *Lower panels*: maximum temperature at the base of the convective envelope (*left*) and maximum TDU parameter (*right*). All values are given with respect to the initial model masses. Black lines and symbols represent cases with no rotation, orange, green, and blue represent, respectively, cases with rotation and $f = 0.1$, 0.15, and 0.2.

3.1. Stellar rotation scenario

We performed a series of evolutionary tests for solar metallicity models with initial masses between 4 and 9.5 $M_{\odot}$ and values of the rotation parameter f (rotation was considered after core He burning) of 0.02, 0.05, 0.1, 0.15, 0.20, and 0.25. They correspond, respectively, to the following $\omega/\omega_{\rm crit}$ values: 0.14, 0.22, 0.32, 0.39, 0.45, and 0.50. In this range of values, we maintain the stability criterion that the ratio of kinetic to gravitational energy remains below 0.14 (Durisen 1975; Kippenhahn et al. 2012), as well as those related to the stability of differential rotation (see Dom96 for a discussion).

We now describe the evolution of the early AGB (E-AGB) and TP-AGB of models leading to UMCO WDs. Given the simplicity of our implementation of rotation, and that a thorough analysis of its effects on intermediate-mass models is beyond the scope of this work, our description merely aims to highlight the main properties of our sequences, and compare them to the results presented in Dom96. The main properties of rotating models leading to UMCO WD and, as a reference, some non-rotating ones of analogous masses, are summarised in Table 1. For the sake of clarity, a selection of these properties is also presented in Fig. 1.

The general behaviour we obtain for models leading to UMCO WD reproduces that described in Dom96. In particular, the lifting effect of rotation in the core leads to a slower increase in the He-burning shell temperature, thus to a slower expansion and decrease in the H-burning shell temperature, and ultimately to a delay in the second dredge-up (SDU), which allows a considerably higher CO core growth. This is inferred from Table 1 and from the top-left panel of Fig. 1, which shows the core mass at the SDU in terms of the initial mass for different rotation parameter values. We also note the resulting larger core masses with increasing f (top-right panel of the same figure). Because of the reduction in maximum temperature induced by core rotation, carbon burning is prevented and the mass of the resulting CO core will be larger than that at which carbon burning is expected in the absence of rotation. As a result, the mass of the degenerate CO core will be larger than 1.05 $M_{\odot}$ before the TP-AGB. By comparing the mass of the H-exhausted core at the end of core He burning ($M_{\rm c,CHeB}$), and the core mass at the maximum advance of the SDU ($M_{\rm c,SDU}$), we can see that rotation even hampers the occurrence of the SDU in our 5 $M_{\odot}$ models. For a comparison, the minimum initial mass for the occurrence of the SDU in non-rotating solar metallicity stars is $\approx$4 $M_{\odot}$ (see e.g., Becker & Iben 1979; Boothroyd & Sackmann 1999).

Table 1. Main characteristics of the TP-(S)AGB of our models leading to UMCO WD.

$M_{\rm ini}$ ($M_\odot$)	TP-AGB	f	$M_{\rm c,CHeB}$ ($M_\odot$)	$M_{\rm c,SDU}$ ($M_\odot$)	$M_{\rm c,f}$ ($M_\odot$)	$M_{\rm env,f}$ ($M_\odot$)	$N_{\rm TP}$	$\tau_{\rm TP\text{-}AGB}$ (Myr)	$\Delta t_{\rm IP}$ (yr)	$T_{\rm BCE}$ (MK)	$L_{\rm max}$ ($10^3\,L_\odot$)	λ	C/O
7.8	VW, SCN	0	1.673	1.016	1.029	1.681	47	0.095	3016	91.5	49.6	0.97	0.34
7.8	VW/10, SCN	0	1.673	1.016	1.066	2.303	406	0.779	2289	95.2	55.3	0.93	2.29
7.8	VW/20, SCN	0	1.673	1.016	1.112	2.732	771	1.107	2283	95.7	57.0	0.92	2.08
7.8	VW/50, SCN	0	1.673	1.016	1.171	4.229	1357	1.431	2274	96.7	63.3	0.93	1.04
7.8	VW, Schw	0	1.709	1.025	1.049	2.352	50	0.086	1727	92.5	50.7	0.62	0.17
7.8	VW/2, Schw	0	1.709	1.025	1.062	2.576	92	0.137	1553	94.2	52.1	0.63	0.22
7.8	VW/5, Schw	0	1.709	1.025	1.102	2.909	234	0.264	1528	96.0	55.1	0.63	0.33
5.0	VW, SCN	0.00	1.036	0.863	0.877	1.405	26	0.193	26222	57.6	26.8	0.94	0.85
5.0	VW, SCN	0.15	1.036	1.036	1.050	1.441	13	0.107	10075	23.9	27.9	0.87	0.58
5.0	VW, SCN	0.20	1.064	1.064	1.105	1.485	12	0.126	12692	17.8	28.0	0.81	0.56
6.0	VW, SCN	0.00	1.268	0.902	0.918	1.632	32	0.201	6581	75.0	34.3	0.96	0.31
6.0	VW, SCN	0.10	1.268	1.060	1.076	1.660	27	0.092	5264	66.4	37.2	0.92	0.55
6.0	VW, SCN	0.15	1.268	1.152	1.168	1.804	21	0.074	4826	57.7	37.7	0.90	0.58
6.0	VW, SCN	0.20	1.268	1.272	1.289	1.817	16	0.056	3984	49.5	39.6	0.84	0.50
7.0	VW, SCN	0.00	1.526	0.972	0.974	2.341	35	0.133	3579	87.0	43.6	0.95	0.30
7.0	VW, SCN	0.05	1.526	1.038	1.054	1.830	34	0.123	3414	84.5	44.6	0.91	0.33
7.0	VW, SCN	0.10	1.526	1.120	1.137	1.755	33	0.117	3336	77.4	48.0	0.91	0.35
7.0	VW, SCN	0.15	1.526	1.224	1.236	2.115	27	0.065	3171	77.4	48.6	0.90	0.29
7.0	VW, SCN	0.20	1.526	1.336	1.350	2.012	22	0.035	4201	73.6	56.7	0.86	0.18
7.5	VW, SCN	0.00	1.591	1.055	1.071	1.849	38	0.102	3741	89.0	46.0	0.97	0.30
7.5	VW, SCN	0.10	1.591	1.134	1.148	1.606	36	0.092	3739	84.9	48.3	0.95	0.37
7.5	VW, SCN	0.15	1.591	1.230	1.245	1.551	33	0.083	3686	84.8	50.4	0.95	0.41
7.8	VW, SCN	0.10	1.684	1.166	1.178	1.752	39	0.084	3066	88.6	52.6	0.93	0.13
7.8	VW, SCN	0.15	1.684	1.265	1.274	1.803	33	0.073	3141	86.7	54.8	0.92	0.31
8.0	VW, SCN	0.00	1.735	1.106	1.116	2.102	45	0.089	3473	94.6	54.5	0.91	0.28
8.0	VW, SCN	0.10	1.735	1.183	1.196	1.768	45	0.087	4306	90.5	55.4	0.91	0.35
8.0	VW, SCN	0.15	1.735	1.281	1.291	1.800	35	0.074	2768	88.7	57.3	0.90	0.35

Notes. For comparative purposes, we also added some selected non-rotating models or altered stellar winds. $M_{\rm ini}$ corresponds to the initial mass. TP-AGB describes the main input physics during this evolutionary stage. VW refers to mass-loss rates by Vassiliadis & Wood (1993), SCN to the implementation of the search for convective neutrality approach to the determination of convective boundaries (see main text for details), and Schw to the implementation of the strict Schwarzschild criterion. f corresponds to the rotation parameter ($f = 0$ means there is no rotation). $M_{\rm c,CHEB}$ and $M_{\rm c,SDU}$ are, respectively, the H-exhausted core masses at the end of core He burning, and at the deepest advance of the second dredge-up. $M_{\rm c,f}$ and $M_{\rm env,f}$ are the final core mass and the H-rich envelope mass left at the end of our calculations. $N_{\rm TP}$, $\tau_{\rm TP\text{-}(S)AGB}$ and $\Delta t_{\rm IP}$ are, respectively, the number of thermal pulses, the duration of the TP-(S)AGB (given from the first thermal pulse until the end of our computations), and the maximum interpulse period in each sequence. $T_{\rm BCE}$, $L_{\rm max}$ and λ are, respectively, the maximum temperature at the base of the convective envelope, the maximum luminosity during the TP-(S)AGB, and the maximum TDU efficiency parameter. C/O is the ratio of final surface number abundances of carbon to oxygen.

The higher WD masses resulting from rotation are in line with recent observational constraints provided by the semi-empirical initial-final mass relation (Cummings et al. 2019). These authors attribute most of the observed scatter of the initial-final mass relation at high initial masses to the occurrence of rotation. Finally, we neglected the effects of rotational mixing during the evolution prior to the AGB phase, starting from the main sequence. This is not a minor simplification, which is expected to lead to higher core masses at the onset of the AGB (Cummings et al. 2019). As a result, the same final core masses can be reached with a lower rotation parameter f on the AGB.

The occurrence of larger H-exhausted cores in rotating models leads to more luminous host stars (see also Dom96). Figure 1 shows how the peak luminosities during the TP-AGB increase with the rotation parameter f. This leads to more efficient stellar winds, to a shorter duration of the TP-AGB phase, and to a decrease in the number of thermal pulses for faster rotating models. As in Dom96, we also obtain that the decrease in effective gravity of the He-exhausted cores of our models also affects the active burning shells and envelope structure, by making them more extended and cooler. Specifically, as f increases, the maximum temperature at the base of the convective envelope ($T_{\rm BCE}$) decreases. Temperatures above $T_{\rm BCE} \gtrsim 3 \times 10^7$ K leads to hot-bottom burning (Boothroyd & Sackmann 1991; Ventura & D'Antona 2005; hereinafter HBB). Its main nucleosynthetic effects reflect the occurrence of the CNO cycle, that is, an increase in surface He and ^{14}N, and a decrease in ^{12}C, and, to a minor extent, in ^{16}O. The $T_{\rm BCE}$ of our 5 $M_\odot$ models computed with rotation are below or just near the threshold for the occurrence of HBB. This is reflected in the high surface C/O values at the end of their evolution, compared to those of more massive models (see Table 1). Indeed, in 5 $M_\odot$ rotating models, ^{12}C is not destroyed by HBB, but efficiently enhanced by the third dredge-up (TDU) episode described below.

Strong HBB, characteristic of intermediate-mass stars hosting the most massive cores, has been considered responsible for the cessation of core growth (Poelarends et al. 2008). However, this effect would be strongly dependant on the modelling of convection. Even though our models hosting the most massive cores do experience more modest core growth during their TP-(S)AGB than their less massive counterparts, we still identify core growth during interpulses. Therefore, we consider that limited overall core growth should be ascribed to shorter TP-(S)AGB lifetimes, combined with efficient TDU.

All our model stars experience the TDU, in which the base of the convective envelope advances inwards and dredges-up

matter previously synthesised in the convective regions associated with thermal pulses. The TDU efficiency is measured by the λ parameter[2]. Its main nucleosynthetic effects are an increase in ^{4}He and ^{12}C, and, to a minor extent, an increase in ^{16}O. The maximum values of λ tend to decrease when f increases, although differences become minor for our most massive models ($M_{\rm ini} \geq 7.5\,M_{\odot}$). The lower efficiency of the TDU with increasing f is related to the relative weakness of the thermal pulses of models with rotation, which, themselves, is caused by their He-burning shell structures being more extended and cooler. For instance, the maximum thermal pulse luminosity, $L_{\rm He}$, for our $7\,M_{\odot}$ models computed with $f = 0$, 0.1, 0.15 and 0.20 are, respectively, 1.59×10^{8}, 1.15×10^{8}, 8.33×10^{7}, and $7.34 \times 10^{7}\,M_{\odot}$. In models without rotation, or in our massive rotating models (those whose initial mass is $\gtrsim$7.5 $M_{\odot}$), λ tends to decrease with increasing initial mass. The reason is that more massive cores are more compact and hotter, $P_{\rm rad}$ is more important in their He-burning shells, and thus degeneracy and thermal pulse strength consequently lower. Because the strength and duration of the instability decreases, the maximum depth of the subsequent TDU episode is also diminished (see Straniero et al. 2003).

The interpulse period of our models (Table 1) does not always follow the trend mentioned by Dominguez et al. (1996) for their 6.8 $M_{\odot}$ non-rotating model. These authors explain that, because of the lower H-burning shell temperatures of rotating models, the critical He mass required for the thermal pulses to occur is reached later, and thus the interpulse period increases with f. In our case, models of initial mass $\leq$7 $M_{\odot}$ present less efficient TDU for higher f cases, which would lead to somewhat more massive He buffers at the beginning of the interpulse. This would, at least partially, balance the need for longer interpulse periods due to the less efficient H-burning shell. In addition, the similarly high $T_{\rm BCE}$ and λ values of our most massive models lead to similar interpulse periods, regardless of the considered f.

We also explored the initial mass boundaries for the formation of WDs of different types. In Table 2, we list the mass of the resulting WD as a function of the initial stellar mass $M_{\rm ini}$ and the rotation parameter f. Black, red, blue, and italic numbers denote, respectively, the evolutionary outcome of normal CO, UMCO, ONe, and WDs with masses exceeding the Chandrasekhar mass value, $M_{\rm Ch}$. We adopted $M_{\rm Ch} = 1.37\,M_{\odot}$, which corresponds to the canonical Chandrasekhar mass expected for non-rotating stars.

Figure 2 illustrates the resulting WD core composition for the set of f values and initial stellar masses we considered. Even for the lowest f value of 0.02, we obtain that the effects of rotation are noticeable and that the formation of UMCO WDs is possible. The range of initial masses leading to UMCO WDs widens as f increases, whereas the range for the formation of ONe-core WDs decreases significantly. Even though the search for $M_{\rm Ch}$ values for rotating models is beyond the scope of the present work, we would like to note at this point that rotation is expected to alter the values of $M_{\rm Ch}$. Anand (1965) used Chandrasekhar's series expansions to show that rotation should increase $M_{\rm Ch}$ by 2%. Ostriker & Bodenheimer (1968) built axisymmetric differentially rotating WD models that could be stable up to masses as high as 4.1 $M_{\odot}$ More recently, using two-dimensional models, Yoon & Langer (2005) confirmed that the critical masses for thermonuclear or ECSN explosions was expected to significantly exceed $M_{\rm Ch}$ in rotating CO cores.

For illustrative purposes, in Fig. 3 we show the internal chemical profiles of our model star of 7.5 $M_{\odot}$ at the TP-AGB for different rotation parameters f. The three models shown have been extracted from the last He flash, so the expected pure He buffer below the H-rich envelope has been diluted by the pulse-driven convection zone, which in turn is responsible for the formation of the intershell rich in He and carbon.

[2] λ is the quotient between the core mass dredged up after a thermal pulse and the core mass increase in the previous interpulse period (see e.g., Mowlavi 1999). High λ values, that is, a very efficient TDU episode, may significantly hamper core growth during the TP-AGB phase.

Table 2. Resulting WD mass as a function of the initial mass $M_{\rm ini}$ and rotation parameter value f for our computed models.

$M_{\rm ini}/M_{\odot}$	f						
	0	0.02	0.05	0.10	0.15	0.20	0.25
4.0	–	–	–	–	0.82	0.93	0.98
5.0	–	–	–	1.02	**1.05**	**1.11**	–
5.5	–	–	–	**1.05**	**1.14**	–	–
6.0	0.90	–	–	**1.08**	**1.17**	**1.29**	**1.34**
7.0	0.97	1.01	**1.05**	**1.14**	**1.24**	**1.35**	*1.48*
7.5	1.02	1.03	**1.07**	**1.15**	**1.25**	–	–
8.0	**1.08**	**1.09**	**1.12**	**1.20**	**1.29**	*1.41*	*1.56*
8.5	**1.16**	**1.17**	**1.18**	**1.25**	**1.35**	–	–
9.0	**1.23**	–	**1.36**	*1.40*	*1.48*	–	–
9.5	**1.35**	–	–	*1.41*	–	–	–

Notes. Black, brown, blue, and italic numbers denote, respectively, the evolutionary outcome of normal CO, UMCO, ONe, and WDs with masses exceeding the Chandrasekhar mass value for non-rotating stars (see also Fig. 2).

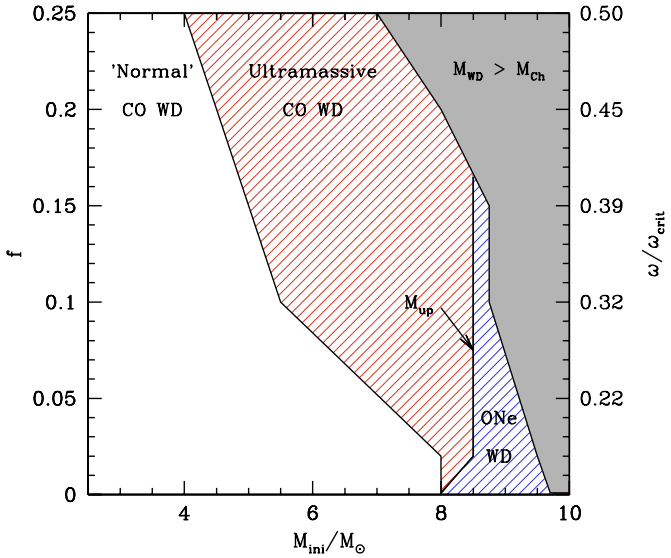

Fig. 2. Evolutionary outcomes for the formation of normal CO, UMCO, and ONe WDs. Rotation parameter f (and equivalent $\omega/\omega_{\rm crit}$) versus initial mass. The adopted value for the Chandrasekhar mass, $M_{\rm Ch}$, corresponds to the canonical value expected for non-rotating stars. $M_{\rm up}$ gives the minimum initial mass threshold that leads to the onset of extended carbon burning.

3.2. Mass-loss scenario

According to existing literature, intermediate-mass stars develop off-centre carbon burning when their degenerate CO cores have

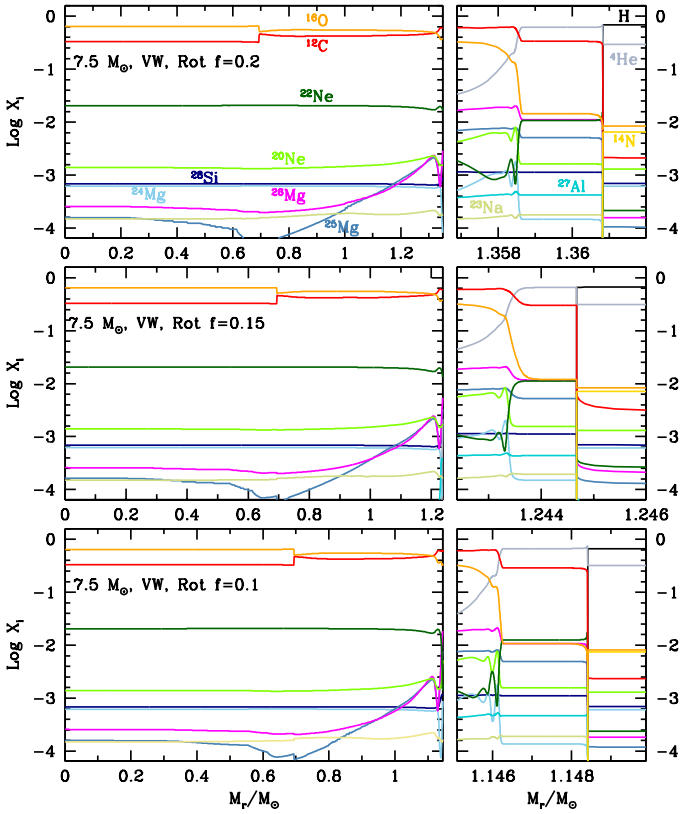

Fig. 3. Inner chemical abundances at the TP-AGB for our 7.5 $M_{\odot}$ initial model for different rotation parameters f and VW mass-loss rates.

a mass $M_{\rm core} \gtrsim 1.05\,M_{\odot}$. The minimum initial mass for this to occur ranges between approximately 6 and 9 $M_{\odot}$ (see Doherty et al. 2017). The degenerate CO cores hosted by stellar models of initial mass below this threshold can still grow beyond the 1.05 $M_{\odot}$ limit during the TP-AGB; however, this growth is typically limited to values of only ∼0.01 $M_{\odot}$ for models of solar and Magellanic Cloud metallicity (see also Fig. 1). The reasons for this limited core growth during the TP-AGB are mainly the strength of stellar winds and the efficiency of the TDU. The initial mass of the core at the beginning of the TP-AGB is determined essentially by the efficiency of the SDU, which depends on the treatment of convection and to a minor extent on the convective boundary mixing (see Wagstaff et al. 2020).

Here, we explore the possibility that UMCO WDs could be formed as a result of a slow growth of the CO core during the TP-AGB. This could be possible as long as the minimum CO-core mass for the occurrence of carbon burning is not reached before the TP-AGB. Indeed, during the TP-AGB, core temperature, which has been increasing since the end of core He burning, starts to decrease, and hence the onset of carbon burning that produces an ONe core is avoided. We carried out this experiment by focusing on a reduction in the mass-loss rates. Specifically, we followed the evolution of an initially 7.8 $M_{\odot}$ model from the ZAMS to advanced stages when the CO core mass had grown above 1.05 $M_{\odot}$ during the TP-AGB.

The efficiency of the TDU is critical to core growth (see Marigo et al. 2020, and references therein) and, ultimately, for the eventual formation of an UMCO WD. Unfortunately, our knowledge of the TDU suffers from uncertainties derived from poorly known input physics, namely, the mixing and the determination of convective boundaries. In order to assess the latter effect, we calculated evolutionary sequences for a 7.8 $M_{\odot}$ initial model using two different prescriptions for the determination of convective boundaries. First, we used the search for convective neutrality (SCN) approach (Castellani et al. 1971; Frost & Lattanzio 1996). The implementation of the SCN has been used successfully in the study of intermediate-mass stars in a wide range of masses and metallicities (see e.g., Karakas & Lattanzio 2014; Doherty et al. 2017, and references therein). The related algorithm aims to limit the effects of the sharp (and unphysical) discontinuity of the radiative gradient at the convective boundaries, and, in practice, it works as an induced overshooting. As a consequence, it favours very efficient TDU, and thus hampers rapid core growth in TP-AGB models.

We also used the Schwarzschild criterion to determine convective boundaries. Naturally, TDU is less efficient, and thus core growth and the formation of UMCO WD models are favoured. Table 1 summarises our main results regarding the effects of stellar winds, which are further discussed below, and those of the determination of convective boundaries. The TDU efficiency, represented by λ, is significantly higher when the SCN is used. When we compare the model computed with standard Vassiliadis & Wood (1993) wind rates and SCN, the model computed with the same wind prescription, and the Schwarzschild criterion (Schw) for convective limits, we see a decrease in λ of ≈36%. It translates in a more massive final H-exhausted core, higher peak luminosities, more efficient stellar winds, and a shorter TP-AGB duration. As a consequence, an UMCO WD can be obtained with a factor-2 decrease in VW mass loss when Schw is used, whereas a decrease in wind rates of a factor slightly lower than 10 is required when SCN is implemented. From the nucleosynthetic point of view, the less efficient TDU obtained with Schw, together with highly efficient HBB, leads to a lower surface abundance C/O ratio.

Asymptotic giant branch winds are probably caused by pulsation-enhanced radiation pressure on carbonaceous or silicate grains present in extended cool envelopes. Collisional coupling between grains and gas allows this gas to be ejected together with grains. Recently, Bladh et al. (2019) studied wind formation and the properties of stellar winds for different stellar masses and luminosities appropriate for the AGB phase by modelling the mass-loss process from first principles, in particular the inclusion of frequency-dependent radiation hydrodynamics and a time-dependent description of dust condensation and evaporation. Their derived mass-loss rates show a large dispersion with input parameters such as stellar luminosity, stellar mass, the abundance of seed particles, grain size, and gas-to-dust mass ratio.

Usually, wind prescriptions in stellar evolution codes are the result of semi-empirical approaches. The mass-loss rates for a part of our computed evolutionary sequence are given in Fig. 4. All the sequences[3], except for the one calculated with standard VW rates, lead to UMCO WDs. Specifically, the cases in which standard rates are reduced by factors of 10, 20, and 50 yield, respectively, degenerate CO-core masses of 1.066, 1.113, and 1.165 $M_{\odot}$. The case in which mass-loss rates are reduced by a factor of 5 leads to a degenerate core of 1.044 $M_{\odot}$, very close to the theoretical mass limit of UMCO WD. The summary of the main characteristics of our sequences computed with different wind rates is shown in Table 1. We mention that our reduced mass-loss rates lead to substantially longer AGB

[3] Some of our sequences reach, towards the end of the TP-AGB phase, an unrealistically high value in the surface luminosity caused by numerical artifacts due to the dominance of radiation pressure at the base of the star envelope.

lifetimes (except when Schw is used, in which case AGB lifetimes are substantially lower) than those provided by observational constraints that support short TP-AGB lifetimes for stars as massive as 4−5 $M_\odot$ (Girardi & Marigo 2007; Pastorelli et al. 2019), thus casting doubt on the use of low mass-loss rate prescriptions with efficient TDU. However, it should be mentioned that these authors extend their analysis up to initial masses of about 5 $M_\odot$, and discard more massive progenitors, which are the ones in which we are interested for our simulations (i.e. progenitors with initial masses larger than 7.5 $M_\odot$).

The comparison with Bladh et al. (2019) is not straightforward, as these authors focused on stars of initial masses up to 3 $M_\odot$, and used a method to derive mass-loss rates different from those of VW. The latter, although relatively simple, has proved successful in reproducing luminosity tips of Magellanic Cloud stars, or surface abundances of AGB stars up to ∼5 $M_\odot$ (Vassiliadis & Wood 1993; Lattanzio & Karakas 2016). However, as noted by Höfner & Olofsson (2018), empirical mass-loss rates expressed as functions of specific variables must be applied with caution, as those variables are affected by other stellar properties and observational biases. Groenewegen et al. (2009) investigated the relation between mass-loss rates, luminosity and dust temperature for an extended sample of LMC and SMC stars. They also adapted their synthetic evolution code to compare theoretical results to observations, and to extend the applicability of VW up to 7.9 $M_\odot$ models. They concluded that, in general, the mass-loss prescription by VW worked well, but pointed to deficiencies in the high $\dot{M}$ range. A recent revision of the latter work by Groenewegen & Sloan (2018) yielded similar results.

Mass-loss determination methods are derived and/or tested through observations. Given the standard initial mass function and the shortness of the duration of the most massive TP-AGB stars, related observations are likely to be far from the mass range of interest in the present work. Mass-loss rate uncertainties may thus be higher for the high mass range of AGB stars. A recent study by Decin et al. (2019) points to the fact that mass-loss rates in OH/IR stars might be overestimated by up to a factor of 100. According to these authors, the presence of undetected companions in extreme OH/IR stars, for which binary frequency is 60−100%, may cause episodes of equatorial density enhancements that might mimic the effects of extreme superwinds. In addition, these authors show that the analysis of low-excitation CO lines is the most reliable method to estimate mass-loss rates in (extreme) OH/IR stars, yielding typical values in the range of $(0.1–3)\times10^{-5}\,M_\odot\,\mathrm{yr}^{-1}$. Our model stars computed with the standard VW experience on average winds between 4 and $7\times10^{-5}\,M_\odot\,\mathrm{yr}^{-1}$ during most of their AGB phase. Thus, they are good candidates to be cases of overestimated mass-loss rates.

Mass-loss rates lower than expected according to current models may not only help to solve the discrepancy between the duration of superwinds (from observations) and the time required for the stars to become WDs (Decin et al. 2019), but also the unexpectedly high masses (≳0.1 $M_\odot$) accreted by C-enhanced metal-poor stars from their companions reported by Abate et al. (2015), the survival of gas planets close to their host stars (Villaver & Livio 2007), or the possibility that planets might shape the planetary nebula of their host star (Hegazi et al. 2020). Moreover, an indication of limitations in how standard models address mass loss and TDU efficiency at higher masses is provided by the semi-empirical initial-final mass relation that predicts a systematic offset of ∼0.1 $M_\odot$ more massive WDs than theoretical models (see Cummings et al. 2018).

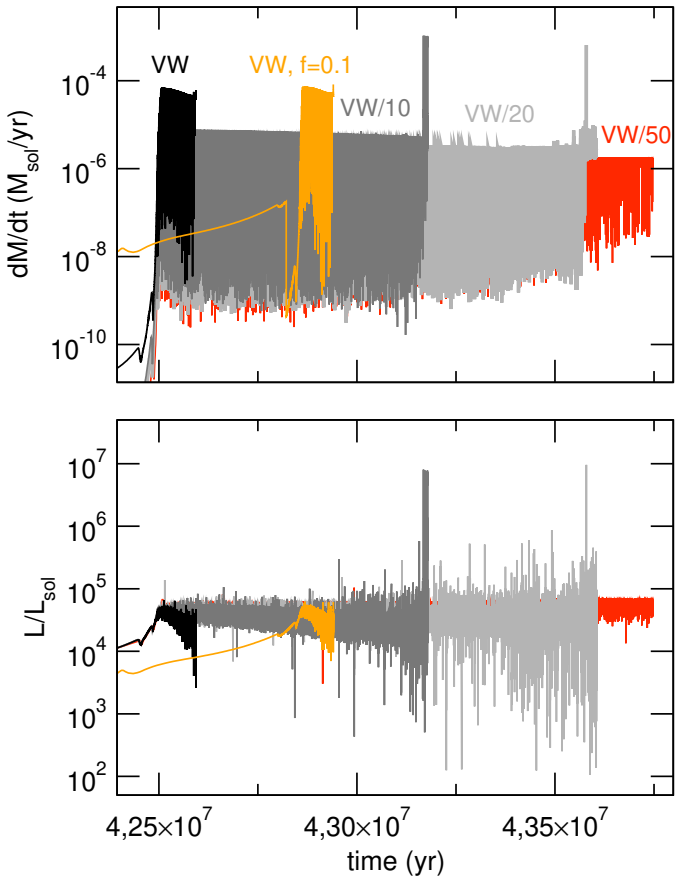

Fig. 4. Mass-loss rates and surface luminosities versus time for models computed with standard VW mass-loss rates (black), standard VW over 10 (dark grey), standard VW over 20 (light grey), standard VW over 50 (red), and standard VW and rotation with $f = 0.1$ (yellow).

We are aware that our reduced-mass-loss scenario is the weakest one to create UMCO WDs. However, this scenario cannot be entirely discarded by different pieces of observational evidence, as we mentioned, including the persisting uncertainties in the efficiency of TDU. Be that as it may, we insist that it constitutes a plausible scenario to identify possible effects of single progenitor evolution on the resulting WD chemical profiles and the impact on its further evolution and observable consequences.

3.3. Double-WD merger scenario

Ultra-massive WDs can also be the result of binary evolution channels, mostly the merger of two intermediate-mass CO-core WDs (WD+WD merger), with a combined mass below the Chandrasekhar limit (see Temmink et al. 2020). Using a detailed, smoothed particle-hydrodynamics code, Dan et al. (2014) presented the merger properties of WD+WD systems and investigated how the components mix chemically. They found that systems with a mass ratio close to unity yield an almost spherical remnant and that the mixing between the components is maximum.

In this study, we considered the formation of an ultra-massive WD resulting from the merger of two equal-mass WDs by assuming the extreme situation of complete mixing between the two WDs and a CO core for the merged remnant. To this end, we adopted the internal distribution of carbon, oxygen, and He of the 0.58 $M_\odot$ WD model computed in Miller Bertolami (2016)

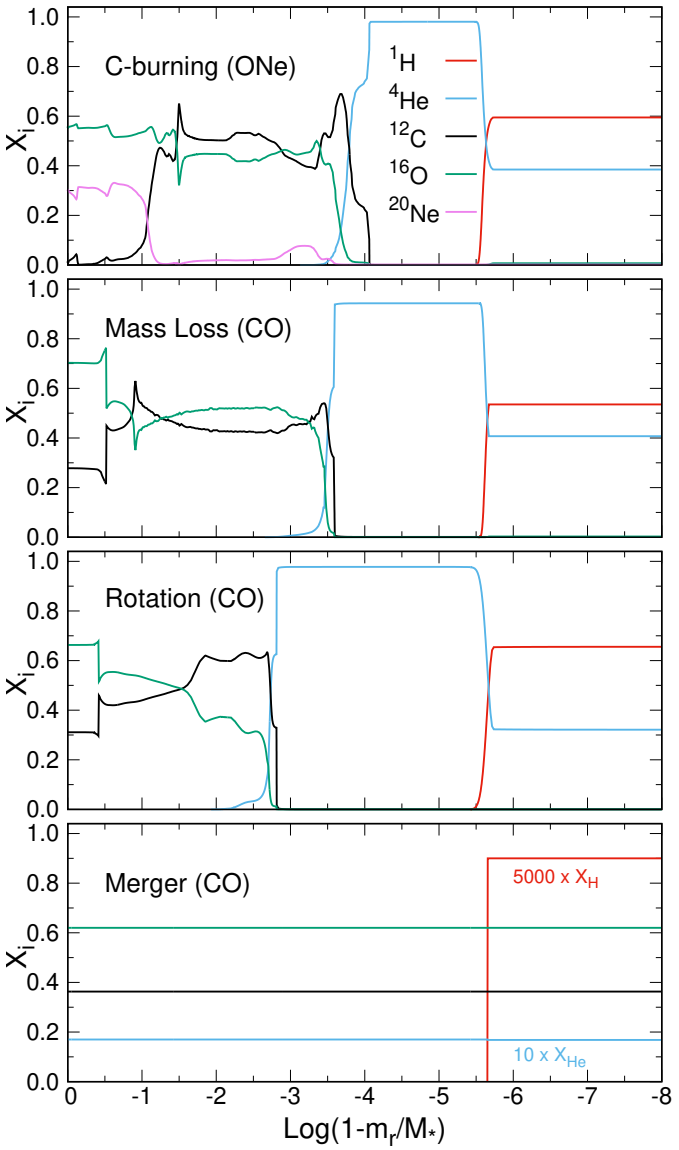

Fig. 5. Internal abundance by mass of selected chemical elements versus the outer mass coordinate for the 1.156 $M_\odot$ WD models resulting from the evolutionary scenarios we studied. *From top to bottom*: ONe WD model from Camisassa et al. (2019), the CO WD model resulting from reduced mass loss during progenitor evolution, the CO WD model implied by rotation, and the merged CO model. Models are shown at the beginning of the cooling track before the core mixing induced by the mean molecular weight inversion.

from the evolutionary history of its progenitor star. Assuming complete mixing between both WDs, the mass fraction of He, carbon and oxygen throughout the interior of our UMCO WD model results $X_{\rm He} = 0.017$, $X_{\rm C} = 0.363$ and $X_{\rm O} = 0.62$. We mention that in this study we are interested in the advanced evolutionary stages of the WD and not the evolutionary stages shortly after the merger event, which cannot be adequately followed by our stellar evolution code. Finally, in this work we did not consider the possibility that WD mergers lead to ultra-massive ONe-core WDs, as predicted in Schwab (2021). The reason is that we do not expect such ONe WDs to present marked differences in their pulsational properties as compared with the ONe-core models resulting from the single evolution that is explored in the present paper.

4. Evolutionary properties

In this section, we compare the evolutionary properties of our UMCO WD models resulting from the two single-evolution scenarios and from the binary merger we described previously, with those predicted by the ONe-core WD models resulting from off-centre carbon burning during the single evolution of the progenitor star (Siess 2010). To isolate the impact of the internal composition predicted by the possible scenarios, we adopted the same stellar mass of 1.159 $M_\odot$ for all of our WD sequences[4]. In addition, we assumed the same H content for all of our sequences except the merger case. In particular, it was taken as nearly the maximum allowed by evolutionary considerations for such stellar mass, $\log(M_{\rm H}/M_\star) \approx -6$. This limit is imposed by the occurrence of unstable nuclear burning on the cooling track for the WD mass considered. Finally, the ONe-core WD-evolutionary and -pulsational models were taken from Camisassa et al. (2019) and De Gerónimo et al. (2019). Such models were computed with the same codes we used to compute the evolution and pulsations of our UMCO WD models (see Sect. 2 for details). The evolutions of all of our WD sequences were followed from very high luminosities, through the domain of the pulsating ZZ Ceti stars, down to very low surface luminosities.

In Fig. 5, we display the internal chemical profile of our UMCO WD models (see Sect. 3 for details), together with the chemical profile of the ONe-core WD model studied in Camisassa et al. (2019), top panel. Specifically, the second and third panels illustrate, respectively, the chemical profiles resulting from reducing the mass-loss rates of an initially 7.8 $M_\odot$ progenitor star, and those from considering core rotation ($f = 0.1$) in the AGB phase of an initially 7.6 $M_\odot$ progenitor star. The bottom panel shows the chemical profile we adopted for our merged WD. The chemical profiles correspond to ultra-massive WD models at the onset of their cooling phase prior to the onset of element diffusion, and before the core mixing implied by the inversion of the mean molecular weight is performed in our simulations.

The chemical structure expected in ultra-massive WDs is markedly different according to the evolutionary scenario that leads to their formation. This is true for both the core and the envelope. The chemical profile that results in the outer part of the CO core is different in the mass-loss and rotation scenarios. The He content of the UMCO WD formed as a result of rotation is larger than that of the UMCO WD formed via reduced mass-loss rates and that of the ONe-core WD. This is because the lower temperature and pressure prompted by core rotation favour the formation of a less degenerate core and thus a larger He content. Since we expect that the internal angular momentum of the core is conserved during the transition from AGB to the hot WD stage, we assume that no He is burnt during the hot stages of WD evolution. We find that when allowing He burning to operate in our non-rotating WD models, the final He content of the WD is reduced. However, even if this is the case, we find that this reduction of the He content does not change the conclusions of our work.

The H content we adopted for our merged WD deserves some comment. Because H is usually not included in smoothed particle-hydrodynamics simulations of double-WD mergers, the amount of H that survives the merger event is roughly inferred (Schwab 2018). It is expected that most of the total initial H will be destroyed by the high temperatures during and after the merger (Dan et al. 2014). In view of the lack of consistent

[4] We do not expect a qualitative change of the conclusions of our work by considering other mass values for the ultra-massive WDs.

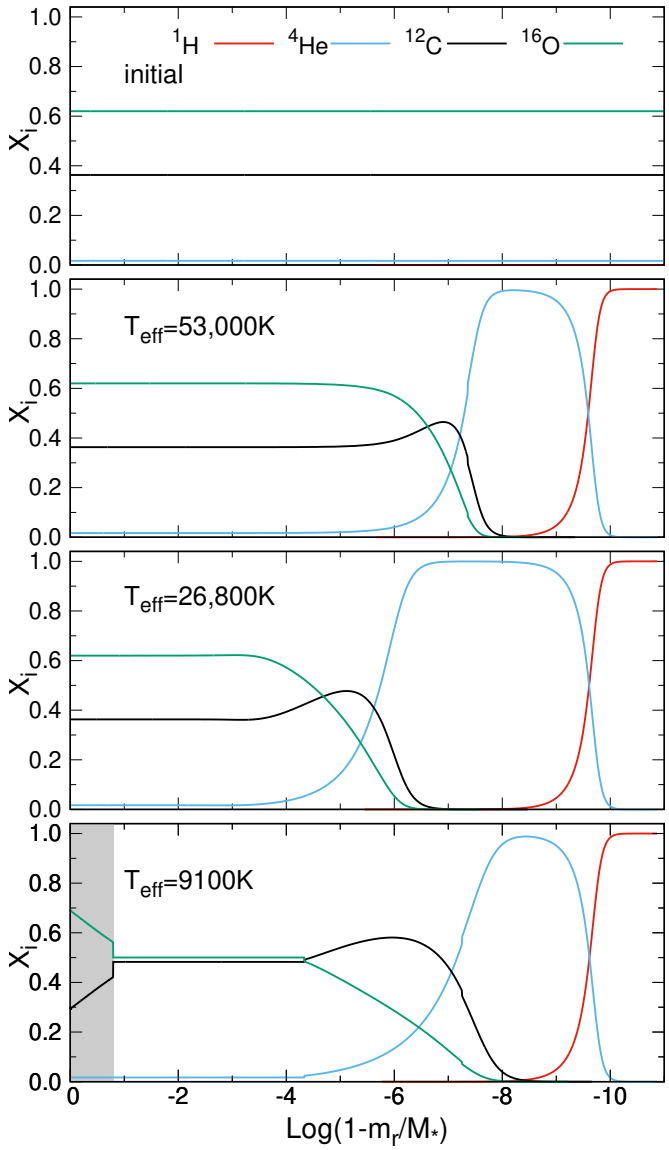

Fig. 6. Internal abundance by mass of H, He, carbon, and oxygen in terms of the outer mass coordinate at various cooling stages of our 1.156 $M_\odot$ UMCO WD sequence resulting from the merger scenario. Each stage is labelled by the effective temperature of the model. The grey area in the *bottom panel* indicates the domain of core crystallisation.

estimations, we inferred the amount of H remaining in our merged WD in a very simple way: assuming complete mixing of the two WDs (see Sect. 3.3), and a H content of $10^{-4}\,M_\odot$ for each WD, the mass fraction of H throughout the 1.156 $M_\odot$ WD results $X_{\rm H} = 2\times10^{-4}\,M_\odot/1.156\,M_\odot = 1.73\times10^{-4}$. At the beginning of the cooling track, H burning occurs in regions below $\log(1-m_{\rm r}/M_{\rm WD}) = -5.6$ in our 1.156 $M_\odot$ WD model. Assuming that all of the H below this layer is burnt, we get the H profile shown in the bottom panel of Fig. 5. The remaining total H content amounts to $5\times10^{-10}\,M_\odot$. For the He distribution, we have assumed no He burning, despite the fact that some burning is expected according to merger simulations (Dan et al. 2014; Katz et al. 2016). We stress again that the chemical stratification we assumed for our merged remnant corresponds to the extreme situation of complete mixing between the two WD components. It is beyond the scope of this paper to analyse other possible situations that would result particularly from the merger of two WD remnants of different masses (Dan et al. 2014).

Three main processes change the internal chemical distribution of our models: the mixing of all core chemical components during the pre-WD and onset of cooling as a result of the inversion of the mean molecular weight, element diffusion during most of WD evolution, and phase separation of core chemical constituents upon crystallisation. Figure 6 illustrates the impact of diffusion and phase separation for the UMCO WD resulting from the merger scenario. Diffusion profoundly changes the abundance distribution of the initial WD model (top panel). In particular, vestiges of inner H surviving the merger episode float to the surface as a result of gravitational settling, thus forming a thin, pure H envelope at rather high effective temperatures. The formation of a pure He buffer below the H envelope is also predicted. At early stages, the mass of this He buffer increases, but as evolution proceeds, chemical diffusion carries He to deeper layers, and the He buffer becomes thinner again (bottom panel). This behaviour can be understood as follows. Generally, the chemical profile in the envelope of a WD is determined by the competition between basically partial pressure gradients, gravity and induced electric field. Diffusion velocities are given by (for simplicity we neglect thermal diffusion):

$$\frac{{\rm d}p_i}{{\rm d}r} + \varrho_i g - n_i Z_i e E = \sum_{j\neq i}^{N} K_{ij}\left(w_j - w_i\right), \tag{2}$$

where, p_i, ϱ_i, n_i, Z_i, and w_i are, respectively, the partial pressure, mass density, number density, mean charge, and diffusion velocity for chemical species i, and g is the gravitational acceleration (Burgers 1969). N is the number of ionic species plus electrons, and K_{ij} are the resistance coefficients. This set of equations is solved together with the equations for no net mass flow $\sum_i A_i n_i w_i = 0$ and no electrical current $\sum_i Z_i n_i w_i = 0$. If we assume only two ionic species with mean charge Z_1 and Z_2 and atomic mass number A_1 and A_2, and consider that electron has zero mass and that ions behave as an ideal gas, then Eq. (2) leads for the diffusion velocity (positive velocity means that element diffuses upwards):

$$K_{12} f_n w_1 = \left(-\frac{A_1}{Z_1} + \frac{A_2}{Z_2}\right) m_{\rm H} g + \left(-\frac{1}{Z_1} + \frac{1}{Z_2}\right) k_{\rm B} T \frac{{\rm d}\ln T}{{\rm d}r} + \frac{k_{\rm B}T}{Z_2}\frac{{\rm d}\ln n_2}{{\rm d}r} - \frac{k_{\rm B}T}{Z_1}\frac{{\rm d}\ln n_1}{{\rm d}r}, \tag{3}$$

where f_n is a positive factor that depends on the number density and atomic charge of species and $m_{\rm H}$ the H-atom mass. The first term on the right-hand side of Eq. (3) takes into account the contribution of gravity (and the influence of the induced electric field) to the diffusion velocity, and the second term gives the contribution of the temperature gradient. These two terms, which are usually referred to as gravitational settling, cause lighter elements to diffuse upwards. The third and fourth terms refer to the chemical diffusion contribution resulting from gradients in number densities. In the case of a mixture of ^{4}He and ^{12}C, the term due to gravity vanishes, and gravitational settling is thus strongly reduced, resulting solely from the contribution due to the temperature gradient, which is responsible for the formation (and thickening) of a pure He buffer, as displayed in Fig. 6. However, as cooling proceeds, temperature gradients in the He/carbon transition zone become smaller and chemical diffusion takes over, causing He to diffuse downwards. This results in a reduction in the He buffer mass at low effective temperatures. In the case of a mixture of H and He the gravity term (first term) does

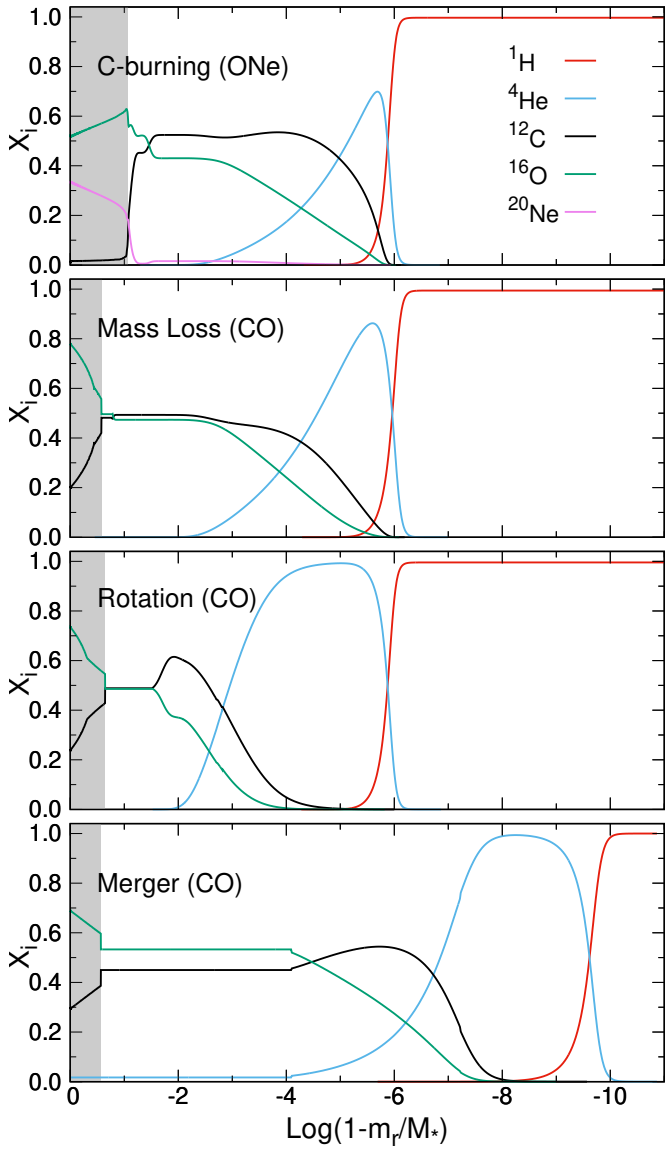

Fig. 7. Same as Fig. 5, but at an effective temperature of $T_{\rm eff}$ = 11 100 K, representative of the domain of pulsating ZZ Ceti stars. The grey area in each panel indicates the domain of core crystallisation.

not vanish, it becomes dominant and causes H to rapidly float to the surface. Finally, the bottom panel shows the imprints of phase separation on the core chemical composition during crystallisation, with the consequent increase of oxygen in the solid core. At this stage, the mass of the crystallised core amounts to about 85%.

The initial chemical profiles of our WD models are substantially altered by the time evolution has proceeded to the domain of the ZZ Ceti instability strip. This is shown in Fig. 7, where it is displayed the internal chemical profile of our ultra-massive 1.156 $M_\odot$ WD models resulting from the four evolutionary scenarios at $T_{\rm eff}$ = 11 100 K. In all the cases, a pure H envelope is formed. Also at this stage, diffusion has strongly smoothed out the initial chemical profile of the WD models, a relevant aspect for pulsational properties (see Sect. 5). For the WD models resulting from the single-evolution scenarios, the initial pure He buffer has been strongly eroded by chemical diffusion. This is because for such scenarios the He buffer was formed in deeper regions (because of the larger H envelopes expected in such cases), where the settling contribution resulting from the temperature gradient becomes smaller. Hence, chemical diffusion dominates, thus causing He to diffuse downwards, and the pure He buffer to disappear. However, we mention that in our treatment of element diffusion, we have not included the effect of Coulomb separation of ions (Chang et al. 2010; Beznogov & Yakovlev 2013), as a result of which ions with larger Z should move to deeper layers. Coulomb diffusion might not be negligible in the dense carbon- and He-rich envelopes of ultra-massive WDs, thus possibly preventing the inward diffusion of He towards the core and leading to a much sharper transition region than we obtained. We checked this issue by artificially assuming that there is no inward chemical diffusion of He, finding that the impact that Coulomb separation could inflict on our pulsational inferences is moderate. Finally, all of our WD models start to crystallise at effective temperatures well above the instability strip, thus keeping a large fraction of their stellar mass crystallised (particularly the ONe-core WD for which Coulomb interactions are larger) when they reach the ZZ Ceti stage. The shape of the chemical profile is modified by crystallisation not only in the growing crystallised core left behind but also in liquid regions beyond the crystallisation front. The changes in the chemical profiles resulting from the phase-separation process strongly impact the theoretical pulsational spectrum and must be taken into account in realistic computations of the pulsational properties of ultra-massive WDs (De Gerónimo et al. 2019).

The evolutionary scenario through which ultra-massive WDs are formed will influence their cooling markedly. This is illustrated in Fig. 8, which compares the cooling times of our UMCO 1.156 $M_\odot$ WD models resulting from reduced mass-loss rates and rotation scenarios, with those of our adopted merged model (dashed, dot dashed, and dotted lines, respectively) and with those corresponding to the ONe-core WD sequence resulting from carbon burning during progenitor evolution (solid line). The cooling times are set to zero at the beginning of the WD cooling phase, when the star reaches the maximum effective temperature. Gravothermal energy is the dominant energy source of the WD. At early stages, for example $\log L/L_\odot \gtrsim -0.7$ ($\log T_{\rm eff} \gtrsim 4.68$), cooling is dictated by energy lost by neutrino emission, which is about the same order of magnitude as the gravothermal energy release. As WDs cool, the temperature of the degenerate core decreases and neutrino luminosity drops. At $-\log L/L_\odot = 2.3-2.5$ ($\log T_{\rm eff} = 4.23-4.28$), crystallisation sets in at the centre of our UMCO WD sequences, resulting in a release of latent heat and gravitational energy due to the phase separation of main-core constituents that impact the cooling times. Because of the larger Coulomb interactions, this occurs when the surface luminosity is higher ($\log L/L_\odot = -2$ ($\log T_{\rm eff} = 4.36$)) for the ONe-core WD sequence, with consequently less relevant impact on the cooling times. Finally, at the lowest luminosities shown in Fig. 8, the temperature of the crystallised core drops below the Debye temperature, and all of the WD sequences enter the so-called Debye cooling phase, which is characterised by a rapid cooling.

Clearly, UMCO WDs evolve slower than the ONe-core WDs. This is due to the larger impact of the energetic of crystallisation in the case of the CO-core WDs and also because the specific heat per gram of CO composition is larger than that of ONe composition. The merged sequence takes the longest to evolve. The main reason for this, apart from the fact that the core of these WD models has the greatest carbon content, is that the He buffer is located at shallower layers than in the other WD sequences. Hence, the layers above the degenerate core are more opaque in the merger WD models (below the WD envelope, carbon opacity

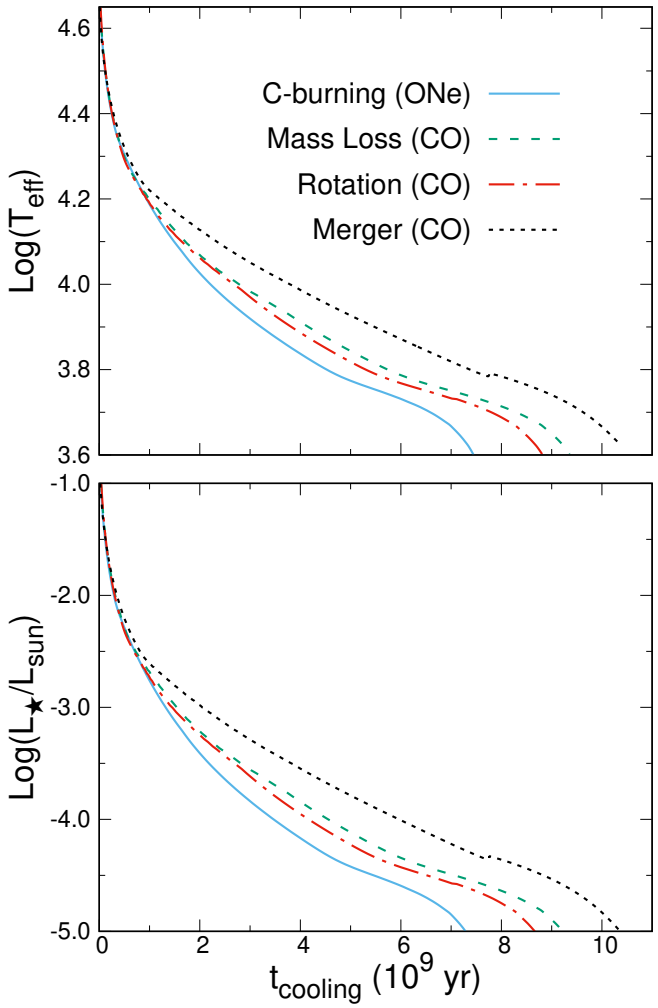

Fig. 8. Effective temperature and surface luminosity (*upper* and *bottom panels*) in terms of the cooling times for our 1.156 $M_\odot$ WD sequences resulting from the various formation scenarios explored in this paper. Cooling time is counted from the time of WD formation.

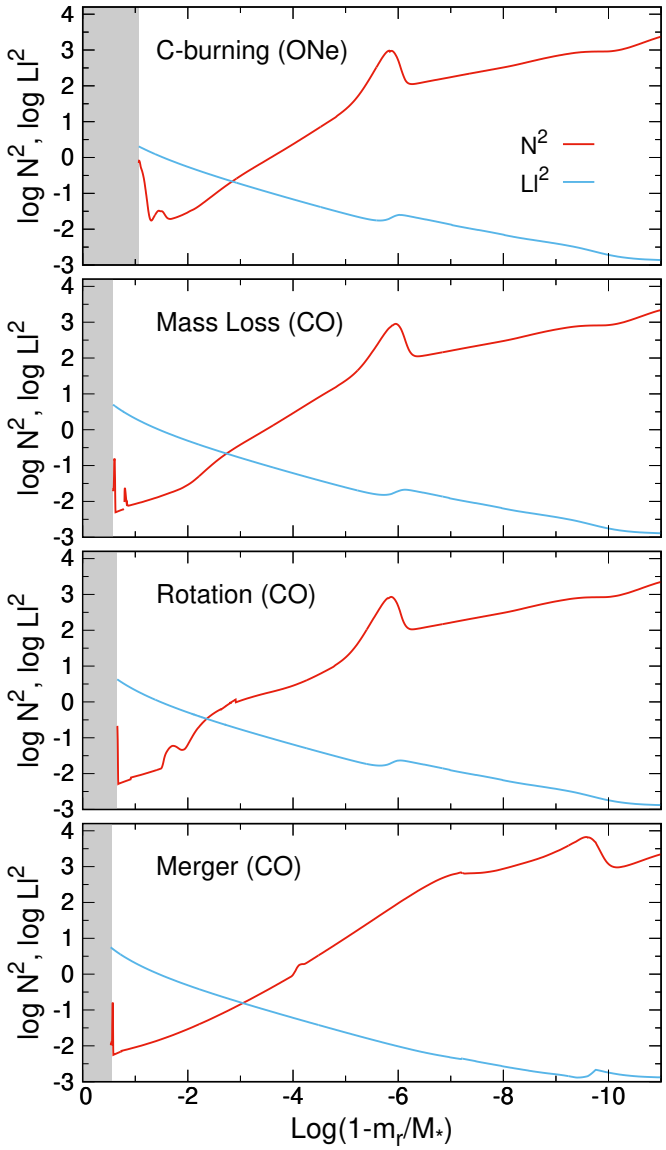

Fig. 9. Same as Fig. 7 but for the logarithm of the squared Brunt–Vaïsälä and Lamb frequencies: red and blue lines, respectively. The Lamb frequency corresponds to dipole ($\ell = 1$) modes. In each panel, the grey area corresponds to the crystallised part of the models.

is larger than that of He), thus slowing the cooling rate. In particular, this sequence takes 1.5 (1.8) times longer to evolve down to $\log L/L_\odot = -3\,(-4)$ than the ONe-core sequence. Finally, at $\log L/L_\odot \sim -4.3$, there is a bump in the cooling curve of the merger sequence. This is a consequence of the convective mixing of the H envelope with the underlying He buffer (the mass fraction of He in the envelope increases up to 80 %). The star initially has an excess of internal energy that has to be radiated to adjust itself to the new He-enriched (more transparent) envelope, with the consequent increase in the cooling time at those stages.

5. Pulsation results

Element diffusion irons out any gradient of chemical composition, translating this into a very smooth shape of the Brunt–Väisälä frequency –the characteristic frequency of pulsation g modes. The shape of the Brunt-Väisälä frequency has a strong impact on the period spectrum and mode-trapping properties of pulsating WDs. The logarithm of the squared Brunt–Väisälä and Lamb[5] frequencies in terms of the outer mass fraction for the 1.156 $M_\odot$ WD models resulting from the various evolutionary scenarios considered in this paper are shown in Fig. 9. The internal chemical profiles of these models are those displayed in Fig. 7. In each case, the grey area corresponds to the crystallised part of the core. In this work, we consider that the eigenfunctions of the g modes cannot penetrate the solid region of the stellar core. For this reason, the propagation region is restricted to the fluid zone, between the edge of the crystallised region and the stellar surface. This implies that any chemical interface located within the crystallised region in each model has no relevance to the pulsation properties of the g modes. In other words, crystallization prevents 'probing' of the internal chemical structure of the solid portion of the core –left by the different formation scenarios of the WD– through the g-mode periods.

In all the cases, there exists a dominant feature in the run of the Brunt–Väisälä frequency associated with the outermost chemical transition region. This chemical transition region corresponds to the ^{4}He-^{1}H interface in the case of the WD model

[5] The Lamb frequency is the critical frequency of pulsation p modes, which has not been detected in pulsating WDs.

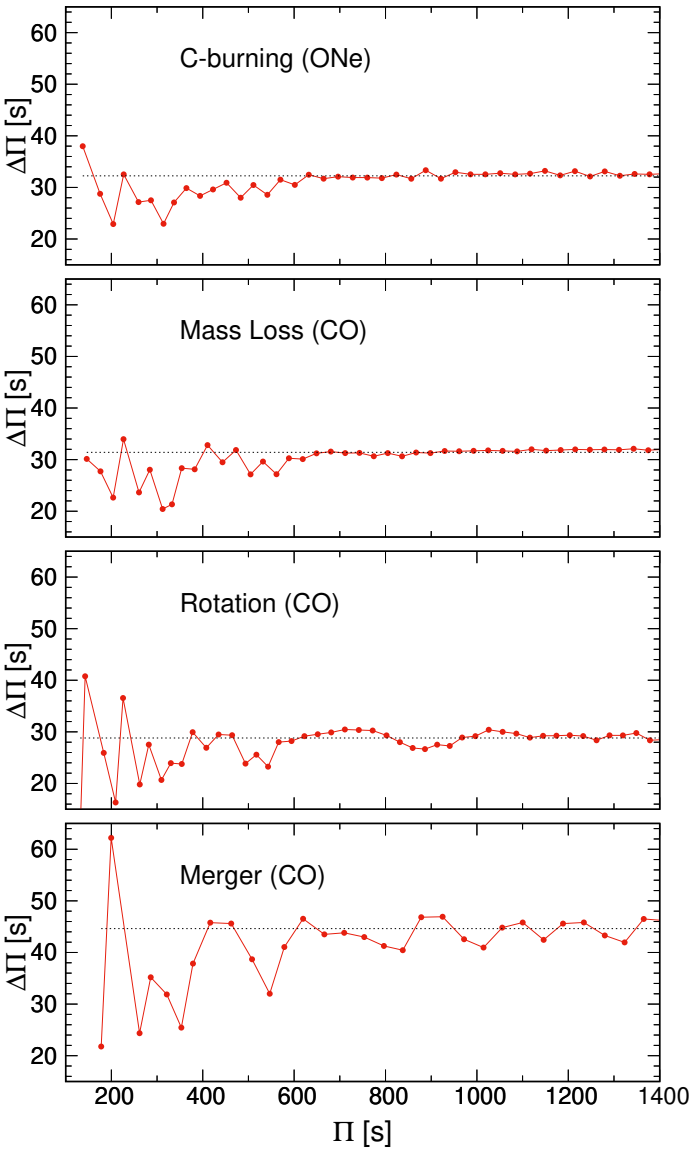

Fig. 10. Same as Fig. 9, but for the forward period spacing ($\Delta\Pi$) in terms of the periods of $\ell = 1$ pulsation g modes. The horizontal black-dashed line is the asymptotic period spacing.

coming from the merger episode, and to the (^{16}O, ^{12}C, ^{4}He)-^{1}H interface for the remaining WD models (see Fig. 7). The bump occurs at a different location for the case of the WD model from the merger [$\log(1-M_{\rm r}/M_\star) \sim -9.5$] than for the other WD models [$\log(1-M_{\rm r}/M_\star) \sim -6$]. The large difference in the spatial location of this bump has significant consequences on the mode-trapping properties of the models. We note the absence of any other bump in the Brunt–Väisälä frequency of the merger model, in contrast to the other models. This implies that for the merger model the mode-trapping properties are determined exclusively by the bump in the fluid zone of the model, that is, the one due to the ^{4}He/^{1}H chemical transition region.

The mode-trapping properties of WDs are dominated by the presence and nature of chemical transitions that are seen as bumps in the Brunt–Väisälä frequency. Specifically, mode trapping manifests itself when at a given $T_{\rm eff}$ value, the separation between consecutive periods departs from the mean (constant) period spacing. A tool for studying the mode-trapping properties in pulsating WDs is the $\Delta\Pi - \Pi$ diagram, in which the separation of periods with consecutive radial order k ('forward period spacing' $\Delta\Pi \equiv \Pi_{k+1} - \Pi_k$) is plotted in terms of the pulsation periods. In Fig. 10, we show the forward period spacing in terms of the periods of $\ell = 1$ pulsation modes for the 1.156 $M_\odot$ CO- and ONe-core WD models considered in Figs. 7 and 9. In all the cases, $\Delta\Pi$ exhibits a regime of short/intermediate periods ($\Pi \lesssim 600$ s) characterised by maxima and minima typical of WD models harbouring one or more chemical interfaces. These maxima and minima represent departures from a constant period separation, which is represented in the figure by the asymptotic period spacing (horizontal black dotted line). For longer periods, the forward period spacing is generally much smoother, without strong signs of mode trapping, and quickly converging to the asymptotic period spacing, except in the case of the WD model coming from the merger scenario, which exhibits notable maxima and minima even for long periods.

A remarkable difference exists in $\Delta\Pi$ between the merged WD and the rest of the WD models. The amplitude of trapping (the magnitude of the maxima and minima of $\Delta\Pi$) is notably larger for this model than for the remaining ones. This difference could be exploited in real ultra-massive ZZ Ceti stars if it were possible to detect several periods with consecutive radial orders as to produce such a diagram, in order to distinguish the origin of the observed WD, that is, to discern whether the star has been formed from a merger episode or is the result of single-star evolution. Another empirical tool to make this distinction could be elaborated on the basis that the average period spacing for the representative WD model of a merger episode is quite larger (∼40%) than for the template models of the other scenarios, as can be seen in Fig. 10. Indeed, a difference of the averaged period spacing of ∼15 s, as our theoretical models of WDs with different origins predict, could be easily detected in ultra-massive ZZ Ceti stars if a sufficient number of periods were detected. This would help to differentiate their possible formation scenarios.

6. Summary and conclusions

We explored two single-star evolution scenarios for the formation of UMCO WDs with stellar masses larger than $M_{\rm WD} \gtrsim 1.05\,M_\odot$. The first of these scenarios involves a reduction in the mass-loss rates usually adopted for the evolution of massive AGB stars. We find that in this case, if the minimum CO-core mass for the occurrence of carbon burning is not reached before the TP-AGB phase, a UMCO WD of mass larger than $M_{\rm WD} \gtrsim 1.05\,M_\odot$ can be formed as a result of the slow growth of CO-core mass during the TP-AGB phase. For this to occur, the mass-loss rates of massive AGB stars need to be reduced by a factor that depends on the poorly known approach to the determination of convection boundaries. Using a search for convective neutrality approach, which favours efficient TDU, imposes the need for mass-loss rates at least 5–20 times lower than standard mass-loss rates. On the other hand, when the strict Schwarzschild criterion is used, the required reduction of standard mass-loss rates drops to a factor of 2. We emphasise that the role of mass loss for the formation of UMCO WDs is conditioned by the efficiency of the TDU. The higher the efficiency of the TDU, the greater the need to decrease mass-loss rates with respect to the standard prescriptions. It follows that the calibration of mass loss is heavily dependent on the treatment of mixing. In addition, this reduction in the mass-loss rates cannot be discarded and is in line with different pieces of recent observational evidence that indicate mass-loss rates lower than expected from current models (e.g., Decin et al. 2019).

The other single-star evolution scenario involves rotation of the degenerate core that results after core He burning at the onset of the AGB phase. We performed a series of evolutionary tests of solar metallicity models of masses between 4 an 9.5 $M_{\odot}$, with core rotation rates f of 0.02, 0.05, 0.1, 0.15, 0.20, and 0.25. As shown in Dom96, we find that the lifting effect of rotation maintains the maximum temperature at lower values than the temperature necessary for off-centre carbon ignition. In addition, the second dredge-up occurs much later than in the case of no rotation. As a result, the mass of the degenerate CO core becomes larger than 1.05 $M_{\odot}$ before the TP-AGB. We find that UMCO WDs can be formed even for values of f as low as 0.02, and that the range of initial masses leading to UMCO WDs widens as f increases, whereas the range for the formation of ONe-core WDs decreases significantly. Finally, we compared our findings with the predictions from ultra-massive WDs resulting from the merger of two equal-mass CO-core WDs, by assuming complete mixing between them and a CO core for the merged remnant.

These two single-evolution scenarios produce UMCO WDs with different CO profiles and different He contents. Element diffusion and phase separation of the CO composition of the core upon crystallisation profoundly alter the initial chemical profiles of resulting UMCO WDs by the time evolution has proceeded to the domain of the ZZ ceti stars. We find that the evolutionary and pulsational properties of the UMCO WDs formed through single-evolution scenarios are markedly different from those of the ONe-core WDs resulting from degenerate carbon burning in single-progenitor stars (see Doherty et al. 2017 for a review), and from those WDs with a carbon-oxygen core that might result from double-degenerate mergers. This can eventually be used to shed light on the core composition of ultra-massive WDs and their origin. UMCO WDs evolve markedly slower than their ONe counterparts[6], with cooling times up to almost a factor of 2 larger. Stellar populations with reliable age inferences could in principle help to discern the origin and core composition of ultra-massive WDs.

Our investigation strongly suggests the formation of UMCO WDs from single stellar evolution. Given recent studies suggesting the formation of ultra-massive WDs with ONe cores after WD merger (Schwab 2021), and the observational demand of the existence of UMCO WDs to explain the large cooling delays of ultra-massive WDs on the Q-branch (Cheng et al. 2020), the formation of UMCO via single evolution we studied in this paper is of utmost interest. In view of the much smaller cooling rates of UMCO WDs with respect to ONe-core WDs, this would have an impact on the predicted mass distribution of massive WDs. Finally, we note that even greater delays in the cooling times of the UMCO WDs are expected if ^{22}Ne sedimentation is considered (see Althaus et al. 2010b; Camisassa et al. 2016). This is so because the diffusion coefficient of ^{22}Ne in the liquid core has a strong dependence on the atomic charge Z of the background matter (Hughto et al. 2010), with the result that ^{22}Ne sedimentation becomes more efficient in a CO-core WD than in a ONe-core WD.

Acknowledgements. We wish to thank the suggestions and comments of an anonymous referee that strongly improved the original version of this work. Part of this work was supported by PIP 112-200801-00940 grant from CONICET, by MINECO grants AYA2014-59084-P, AYA2017-86274-P, and PID2019-109363GB-I00/AEI/10.13039/501100011033, by grant G149 from University of La Plata, and by the AGAUR grant SGR-661/201. ARM acknowledges support from the MINECO under the Ramón y Cajal programme (RYC-2016-20254). This research has made use of NASA Astrophysics Data System.

[6] The evolutionary sequences are available at http://evolgroup.fcaglp.unlp.edu.ar/TRACKS/tracks.html

References

Abate, C., Pols, O. R., Karakas, A. I., & Izzard, R. G. 2015, A&A, 576, A118
Althaus, L. G., Serenelli, A. M., Córsico, A. H., & Montgomery, M. H. 2003, A&A, 404, 593
Althaus, L. G., Serenelli, A. M., Panei, J. A., et al. 2005, A&A, 435, 631
Althaus, L. G., Córsico, A. H., Isern, J., & García-Berro, E. 2010a, A&ARv, 18, 471
Althaus, L. G., García-Berro, E., Renedo, I., et al. 2010b, ApJ, 719, 612
Althaus, L. G., Camisassa, M. E., Miller Bertolami, M. M., Córsico, A. H., & García-Berro, E. 2015, A&A, 576, A9
Althaus, L. G., Córsico, A. H., Uzundag, M., et al. 2020, A&A, 633, A20
Anand, S. P. S. 1965, Proc. Natl. Acad. Sci., 54, 23
Beaudet, G., & Tassoul, M. 1971, A&A, 13, 209
Becker, S. A., & Iben, I., Jr. 1979, ApJ, 232, 831
Beznogov, M. V., & Yakovlev, D. G. 2013, Phys. Rev. Lett., 111, 161101
Bladh, S., Liljegren, S., Höfner, S., Aringer, B., & Marigo, P. 2019, A&A, 626, A100
Boothroyd, A. I., & Sackmann, I. J. 1991, J. R. Astron. Soc. Can., 85, 204
Boothroyd, A. I., & Sackmann, I. J. 1999, ApJ, 510, 232
Burgers, J. M. 1969, Flow Equations for Composite Gases (New York: Academic Press)
Camisassa, M. E., Althaus, L. G., Córsico, A. H., et al. 2016, ApJ, 823, 158
Camisassa, M. E., Althaus, L. G., Rohrmann, R. D., et al. 2017, ApJ, 839, 11
Camisassa, M. E., Althaus, L. G., Córsico, A. H., et al. 2019, A&A, 625, A87
Campbell, S. W., & Lattanzio, J. C. 2008, A&A, 490, 769
Cannon, R. C. 1993, MNRAS, 263, 817
Cantiello, M., Mankovich, C., Bildsten, L., Christensen-Dalsgaard, J., & Paxton, B. 2014, ApJ, 788, 93
Castanheira, B. G., Kepler, S. O., Kleinman, S. J., Nitta, A., & Fraga, L. 2010, MNRAS, 405, 2561
Castanheira, B. G., Kepler, S. O., Kleinman, S. J., Nitta, A., & Fraga, L. 2013, MNRAS, 430, 50
Castellani, V., Giannone, P., & Renzini, A. 1971, Ap&SS, 10, 340
Chang, P., Bildsten, L., & Arras, P. 2010, ApJ, 723, 719
Cheng, S., Cummings, J. D., Ménard, B., & Toonen, S. 2020, ApJ, 891, 160
Christensen-Dalsgaard, J., Silva Aguirre, V., Cassisi, S., et al. 2020, A&A, 635, A165
Córsico, A. H., & Althaus, L. G. 2006, A&A, 454, 863
Córsico, A. H., García-Berro, E., Althaus, L. G., & Isern, J. 2004, A&A, 427, 923
Córsico, A. H., Althaus, L. G., Montgomery, M. H., García-Berro, E., & Isern, J. 2005, A&A, 429, 277
Córsico, A. H., Althaus, L. G., Miller Bertolami, M. M., & Kepler, S. O. 2019a, A&ARv, 27, 7
Córsico, A. H., De Gerónimo, F. C., Camisassa, M. E., & Althaus, L. G. 2019b, A&A, 632, A119
Cummings, J. D., Kalirai, J. S., Tremblay, P. E., Ramirez-Ruiz, E., & Choi, J. 2018, ApJ, 866, 21
Cummings, J. D., Kalirai, J. S., Choi, J., et al. 2019, ApJ, 871, L18
Curd, B., Gianninas, A., Bell, K. J., et al. 2017, MNRAS, 468, 239
Cyburt, R. H., Amthor, A. M., Ferguson, R., et al. 2010, ApJS, 189, 240
Dan, M., Rosswog, S., Brüggen, M., & Podsiadlowski, P. 2014, MNRAS, 438, 14
Decin, L., Homan, W., Danilovich, T., et al. 2019, Nat. Astron., 3, 462
De Gerónimo, F. C., Córsico, A. H., Althaus, L. G., Wachlin, F. C., & Camisassa, M. E. 2019, A&A, 621, A100
Denissenkov, P. A., Herwig, F., Truran, J. W., & Paxton, B. 2013, ApJ, 772, 37
Doherty, C. L., Siess, L., Lattanzio, J. C., & Gil-Pons, P. 2010, MNRAS, 401, 1453
Doherty, C. L., Gil-Pons, P., Lau, H. H. B., et al. 2014, MNRAS, 441, 582
Doherty, C. L., Gil-Pons, P., Siess, L., & Lattanzio, J. C. 2017, PASA, 34, e056
Dominguez, I., Straniero, O., Tornambe, A., & Isern, J. 1996, ApJ, 472, 783
Dunlap, B. H., & Clemens, J. C. 2015, in 19th European Workshop on White Dwarfs, eds. P. Dufour, P. Bergeron, & G. Fontaine, ASP Conf. Ser., 493, 547
Durisen, R. H. 1975, ApJ, 199, 179
Espinosa Lara, F., & Rieutord, M. 2013, A&A, 552, A35
Farmer, R., Fields, C. E., & Timmes, F. X. 2015, ApJ, 807, 184
Fontaine, G., & Brassard, P. 2008, PASP, 120, 1043
Frost, C. A., & Lattanzio, J. C. 1996, ApJ, 473, 383
Gagnier, D., Rieutord, M., Charbonnel, C., Putigny, B., & Espinosa Lara, F. 2019, A&A, 625, A89
García-Berro, E., & Iben, I. 1994, ApJ, 434, 306
García-Berro, E., Ritossa, C., & Iben, I., Jr. 1997, ApJ, 485, 765

Georgy, C., Ekström, S., Granada, A., et al. 2013, A&A, 553, A24
Gil-Pons, P., Suda, T., Fujimoto, M. Y., & García-Berro, E. 2005, A&A, 433, 1037
Gil-Pons, P., Doherty, C. L., Lau, H., et al. 2013, A&A, 557, A106
Gil-Pons, P., Doherty, C. L., Gutiérrez, J. L., et al. 2018, PASA, 35, 38
Girardi, L., & Marigo, P. 2007, A&A, 462, 237
Grevesse, N., Noels, A., & Sauval, A. J. 1996, in Cosmic Abundances, eds. S. S. Holt, & G. Sonneborn, ASP Conf. Ser., 99, 117
Groenewegen, M. A. T., & Sloan, G. C. 2018, A&A, 609, A114
Groenewegen, M. A. T., Sloan, G. C., Soszyński, I., & Petersen, E. A. 2009, A&A, 506, 1277
Hale, S. E., Champagne, A. E., Iliadis, C., et al. 2002, Phys. Rev. C, 65, 015801
Hale, S. E., Champagne, A. E., Iliadis, C., et al. 2004, Phys. Rev. C, 70, 045802
Hegazi, A., Bear, E., & Soker, N. 2020, MNRAS, 496, 612
Heger, A., & Langer, N. 2000, ApJ, 544, 1016
Hermes, J. J., Kepler, S. O., Castanheira, B. G., et al. 2013, ApJ, 771, L2
Herwig, F., Langer, N., & Lugaro, M. 2003, ApJ, 593, 1056
Höfner, S., & Olofsson, H. 2018, A&ARv, 26, 1
Hollands, M. A., Tremblay, P. E., Gänsicke, B. T., et al. 2020, Nat. Astron., 4, 663
Horowitz, C. J., Schneider, A. S., & Berry, D. K. 2010, Phys. Rev. Lett., 104, 231101
Hughto, J., Schneider, A. S., Horowitz, C. J., & Berry, D. K. 2010, Phys. Rev. E, 82, 066401
Iglesias, C. A., & Rogers, F. J. 1996, ApJ, 464, 943
Iliadis, C., D'Auria, J. M., Starrfield, S., Thompson, W. J., & Wiescher, M. 2001, ApJS, 134, 151
Jiménez-Esteban, F. M., Torres, S., Rebassa-Mansergas, A., et al. 2018, MNRAS, 480, 4505
Jorissen, A., & Arnould, M. 1989, A&A, 221, 161
Kanaan, A., Nitta, A., Winget, D. E., et al. 2005, A&A, 432, 219
Karakas, A. I., & Lattanzio, J. C. 2014, PASA, 31, e030
Karakas, A. I., Lugaro, M. A., Wiescher, M., Görres, J., & Ugalde, C. 2006, ApJ, 643, 471
Katz, M. P., Zingale, M., Calder, A. C., et al. 2016, ApJ, 819, 94
Kepler, S. O., Pelisoli, I., Koester, D., et al. 2016, MNRAS, 455, 3413
Kippenhahn, R., Meyer-Hofmeister, E., & Thomas, H. C. 1970, A&A, 5, 155
Kippenhahn, R., Weigert, A., & Weiss, A. 2012, Stellar Structure and Evolution (Berlin, Heidelberg: Springer-Verlag)
Kleinman, S. J., Kepler, S. O., Koester, D., et al. 2013, ApJS, 204, 5
Lattanzio, J., & Karakas, A. 2016, J. Phys. Conf. Ser., 728, 022002
Lederer, M. T., & Aringer, B. 2009, A&A, 494, 403
Limongi, M., & Chieffi, A. 2018, ApJS, 237, 13
Lorén-Aguilar, P., Isern, J., & García-Berro, E. 2009, A&A, 500, 1193
Lugaro, M., Herwig, F., Lattanzio, J. C., Gallino, R., & Straniero, O. 2003, ApJ, 586, 1305
Lugaro, M., Ugalde, C., Karakas, A. I., et al. 2004, ApJ, 615, 934
Maeder, A., & Meynet, G. 2000, ARA&A, 38, 143
Maoz, D., Hallakoun, N., & Badenes, C. 2018, MNRAS, 476, 2584
Marigo, P., & Aringer, B. 2009, A&A, 508, 1539
Marigo, P., Cummings, J. D., Curtis, J. L., et al. 2020, Nat. Astron., 4, 1102
Medin, Z., & Cumming, A. 2010, Phys. Rev. E, 81, 036107
Miller Bertolami, M. M. 2016, A&A, 588, A25
Montgomery, M. H., & Winget, D. E. 1999, ApJ, 526, 976
Mowlavi, N. 1999, A&A, 344, 617
Ostriker, J. P., & Bodenheimer, P. 1968, ApJ, 151, 1089
Pastorelli, G., Marigo, P., Girardi, L., et al. 2019, MNRAS, 485, 5666
Paxton, B., Smolec, R., Schwab, J., et al. 2019, ApJS, 243, 10
Poelarends, A. J. T., Herwig, F., Langer, N., & Heger, A. 2008, ApJ, 675, 614
Rebassa-Mansergas, A., Rybicka, M., Liu, X. W., Han, Z., & García-Berro, E. 2015, MNRAS, 452, 1637
Reimers, D. 1975, Mem. Soc. R. Sci. Liege, 8, 369
Reindl, N., Schaffenroth, V., Miller Bertolami, M. M., et al. 2020, A&A, 638, A93
Rohrmann, R. D. 2018, MNRAS, 473, 457
Rohrmann, R. D., Althaus, L. G., García-Berro, E., Córsico, A. H., & Miller Bertolami, M. M. 2012, A&A, 546, A119
Rowan, D. M., Tucker, M. A., Shappee, B. J., & Hermes, J. J. 2019, MNRAS, 486, 4574
Salaris, M., Althaus, L. G., & García-Berro, E. 2013, A&A, 555, A96
Schwab, J. 2018, MNRAS, 476, 5303
Schwab, J. 2021, ApJ, 906, 53
Shen, K. J., Bildsten, L., Kasen, D., & Quataert, E. 2012, ApJ, 748, 35
Siess, L. 2006, A&A, 448, 717
Siess, L. 2007, A&A, 476, 893
Siess, L. 2010, A&A, 512, A10
Silva Aguirre, V., Christensen-Dalsgaard, J., Cassisi, S., et al. 2020, A&A, 635, A164
Straniero, O., Domínguez, I., Cristallo, S., & Gallino, R. 2003, PASA, 20, 389
Tassoul, M., Fontaine, G., & Winget, D. E. 1990, ApJS, 72, 335
Temmink, K. D., Toonen, S., Zapartas, E., Justham, S., & Gänsicke, B. T. 2020, A&A, 636, A31
Toonen, S., Hollands, M., Gänsicke, B. T., & Boekholt, T. 2017, A&A, 602, A16
Vassiliadis, E., & Wood, P. R. 1993, ApJ, 413, 641
Ventura, P., & D'Antona, F. 2005, A&A, 431, 279
Ventura, P., & D'Antona, F. 2011, MNRAS, 410, 2760
Villaver, E., & Livio, M. 2007, ApJ, 661, 1192
Wagstaff, G., Miller Bertolami, M. M., & Weiss, A. 2020, MNRAS, 493, 4748
Winget, D. E., & Kepler, S. O. 2008, ARA&A, 46, 157
Wood, P. R., & Faulkner, D. J. 1987, Proc. Astron. Soc. Aust., 7, 75
Yoon, S. C., & Langer, N. 2005, A&A, 435, 967
Yoon, S. C., Podsiadlowski, P., & Rosswog, S. 2007, MNRAS, 380, 933